JOURNAL OF PETROLOGY | VOLUME 49 | NUMBER 5 | PAGES 937–970 | 2008 | doi:10.1093/petrology/egn012

Petrology and U–Pb Zircon Geochronology of Amphibole-rich Cumulates with Sanukitic Affinity from Husky Ridge (Northern Victoria Land, Antarctica): Insights into the Role of Amphibole in the Petrogenesis of Subduction-related Magmas

MASSIMO TIEPOLO[1]* AND RICCARDO TRIBUZIO[1,2]

[1]CNR–ISTITUTO DI GEOSCIENZE E GEORISORSE, U.O. DI PAVIA, VIA FERRATA 1, I27100 PAVIA, ITALY
[2]DIPARTIMENTO DI SCIENZE DELLA TERRA, UNIVERSITÀ DI PAVIA, VIA FERRATA 1, I27100 PAVIA, ITALY

RECEIVED MAY 14, 2007; ACCEPTED FEBRUARY 18, 2008
ADVANCE ACCESS PUBLICATION APRIL 9, 2008

A microanalytical trace element and geochronological study was carried out on mafic amphibole-rich cumulates (quartz diorites) cropping out in northern Victoria Land (Antarctica). Associated tonalites and basement rocks were also investigated. Rock textures and major and trace element mineral compositions reveal the presence in quartz diorites of two mineral assemblages: (1) clinopyroxene-I + brown amphibole ± dark mica; (2) clinopyroxene-II + green amphibole + plagioclase + quartz. Both mineral assemblages contain mafic phases with elevated Mg-number, but their trace element signatures differ significantly. In situ *U–Pb zircon geochronology was carried out to support petrogenetic and geological interpretations. Quartz diorites were emplaced in the mid-crust probably at 516 ± 3 Ma. Parental melts of quartz diorites were computed by applying solid/liquid partition coefficients. The melt in equilibrium with the first mineral assemblage (melt-I) is extremely depleted in heavy rare earth elements (HREE), Y, Ti, Zr and Hf (at about 0·2 times normal mid-ocean ridge basalt) and enriched in B, Th, U, the large ion lithophile elements and light REE (LREE). It shares many similarities with sanukitic melts (e.g. Setouchi andesites), which originated by equilibration of subduction-derived sediment melts with a refractory mantle. The melt in equilibrium with the second mineral assemblage (melt-II) is characterized by a steep LREE enrichment (La_N/Yb_N up to 39), a U-shaped HREE pattern and low Ti, which is depleted relative to HREE. The trace element signature of melt-II can be acquired through amphibole crystallization starting from a sanukitic melt similar to melt-I, probably in a deeper magma chamber. Our results allow us to constrain that melts from the subducted slab were produced on a regional scale, in accordance with literature data, below a large sector of the east Gondwana margin during the mid-Cambrian. Implications for the role of amphibole in petrogenesis of subduction-related magmas are also discussed.*

KEY WORDS: *amphibole; sanukite; high-Mg andesites; Ross Orogeny; Antarctica*

INTRODUCTION

Most studies on primary melt composition in modern and fossil active margins are carried out on volcanic rocks, which represent only a portion of the magmatism produced during a collisional event, as melts may stall at different levels within the crust. In addition, the low-pressure mineral assemblage found in volcanic rocks may not represent that of mid- to high-pressure conditions, which mostly controls the evolution of the magma suite

*Corresponding author. E-mail: tiepolo@crystal.unipv.it

(Davidson *et al.*, 2007). Petrological and geochemical information from volcanic rocks alone is thus not fully instructive about the petrogenetic processes and their variation during convergent tectonics and magmatism. The importance of mafic and ultramafic intrusive rocks in yielding additional constraints on petrogenetic processes at the origin of subduction-related magmatism has been recently shown, for instance, in the well-exposed sections of the arc lower crust of Kohistan (Pakistan, Garrido *et al.*, 2006; Jagoutz *et al.*, 2006) and Talkeetna (Alaska, Greene *et al.*, 2006). Mafic and ultramafic intrusive rocks exposed along orogenic belts may thus be important sources of information on hidden crustal processes that occurred during the subduction event. These rocks locally preserve relict mineral phases or complex zoning that is the record of variations in magma composition (e.g. Blundy & Shimizu, 1991; Tiepolo & Tribuzio, 2005). Petrological results, when coupled with age patterns from *in situ* U–Pb analyses, may provide the timing of the different magmatic events and important constraints for the evolution of an orogen (Giacomini *et al.*, 2007).

Increasing attention has been recently paid to amphibole-rich mafic intrusive rocks. Many arc lavas seem to be residual after amphibole crystallization but rarely they carry gabbroic crustal xenoliths in which amphibole is a dominant mineral phase. It is supposed that a cryptic amphibole crystallization at mid-crustal depths occurs in subduction-related contexts (Davidson *et al.*, 2007). The presence of large volumes of amphibole cumulates at mid-crustal levels has also implications for the H_2O budget in arc crust because of the capability of amphibole to act as a 'sponge' (Davidson *et al.*, 2007). Amphibole crystallization has been also proposed, together with minor garnet, to account for the steep light rare earth element (LREE) enrichment of adakites (Macpherson *et al.*, 2006; Rodriguez *et al.*, 2007).

Amphibole-rich intrusive rocks are exhumed along many orogenic belts. Examples are, for instance, the hornblendites and amphibole-rich gabbros of the Adamello batholith and the Bregaglia intrusion in the Italian Alps (Tiepolo *et al.*, 2002; Tiepolo & Tribuzio, 2005), the quartz melagabbros from the Glenelg River Complex in the Delamerian Orogen of Australia (Kemp, 2003, 2004) and the high-Mg diorites in Kyushu, Japan (Kamei *et al.*, 2004). The involvement of high-Mg andesite (HMA) melts with adakitic, boninitic or sanukitic affinity was proposed for the origin of these amphibole-rich mafic intrusive rocks. Adakites are HMA with high La_N/Yb_N ratios (>10) and high Sr contents (>400 ppm) formed by partial melting of the subducted slab in eclogite facies (Drummond & Defant, 1990). Boninites are HMA extremely depleted in high field strength elements (HFSE) and heavy rare earth elements [e.g. HREE at about 0·01 normal mid-ocean ridge basalt (N-MORB)] characterized by large ion lithophile element (LILE) enrichment. Their origin is commonly attributed to high-temperature partial melting of a refractory mantle wedge (Crawford *et al.*, 1989); in particular, the LILE enrichment is related to the addition of a H_2O-rich component from the dehydration of the subducted slab (e.g. Pearce *et al.* 1992). Sanukitoids are Archaean high-Mg diorites with modern analogues in the Setouchi Volcanic Belt HMA. They share similarities with the low-SiO_2 adakites and are characterized by strong LILE and LREE enrichments, low HREE contents, high Cr and Ni, and Mg-number $\gg$ 0·62 (Martin *et al.*, 2005). The petrogenesis of Setouchi andesites is related to the equilibrium reaction of a mantle peridotite with silicic liquids derived from the partial melting of the subducted sediments (Shimoda *et al.*, 1998).

At the Husky Ridge locality, in the northern Victoria Land sector of the Ross Orogen (Antarctica), amphibole-rich mafic cumulates are exposed. The knowledge of the geochemical signature of mantle-derived melts along this section of Gondwana during the Ross Orogeny is fragmentary and poorly constrained in time. The nearby mafic–ultramafic layered sequence from Niagara Icefall has been recently shown to have formed from boninite-type melts (Tribuzio *et al.*, 2007). Conversely, most available literature on subduction-related magmatic products deals with dioritic to granitoid rocks that record extensive crustal contamination (Dallai *et al.*, 2003; Rocchi *et al.*, 2004).

An *in situ* geochemical and geochronological study was therefore carried out on the mafic amphibole-rich cumulates and associated rocks cropping out at the Husky Ridge locality. These rocks represent an important record to: (1) constrain the composition and affinity of the mantle melts developed during the Ross Orogeny in this sector of Gondwana; (2) unravel the petrogenetic processes at the origin of the amphibole-rich intrusive rocks; (3) explore the role of amphibole during arc magma evolution; that is, its capability to give residual melts with steep REE patterns, typical of adakitic melts.

GEOLOGICAL SETTING AND FIELD RELATIONS

The Ross–Delamerian Orogen is broadly the result of the subduction of the Palaeo-Pacific oceanic plate beneath the continental margin of Gondwana during the Early Palaeozoic (e.g. Cooper & Tulloch, 1992; Münker & Crawford, 2000; Boger & Miller, 2004; Foster *et al.*, 2005). It is at present represented by a belt extending from southeastern Australia to the margin of the East Antarctic craton (e.g. Borg & DePaolo, 1991; Stump, 1995; Rocchi *et al.*, 1998). The Transantarctic Mountains extend across the entire Antarctic continent and represent the uplifted basement of the Ross Orogen (Stump, 1995). The oldest

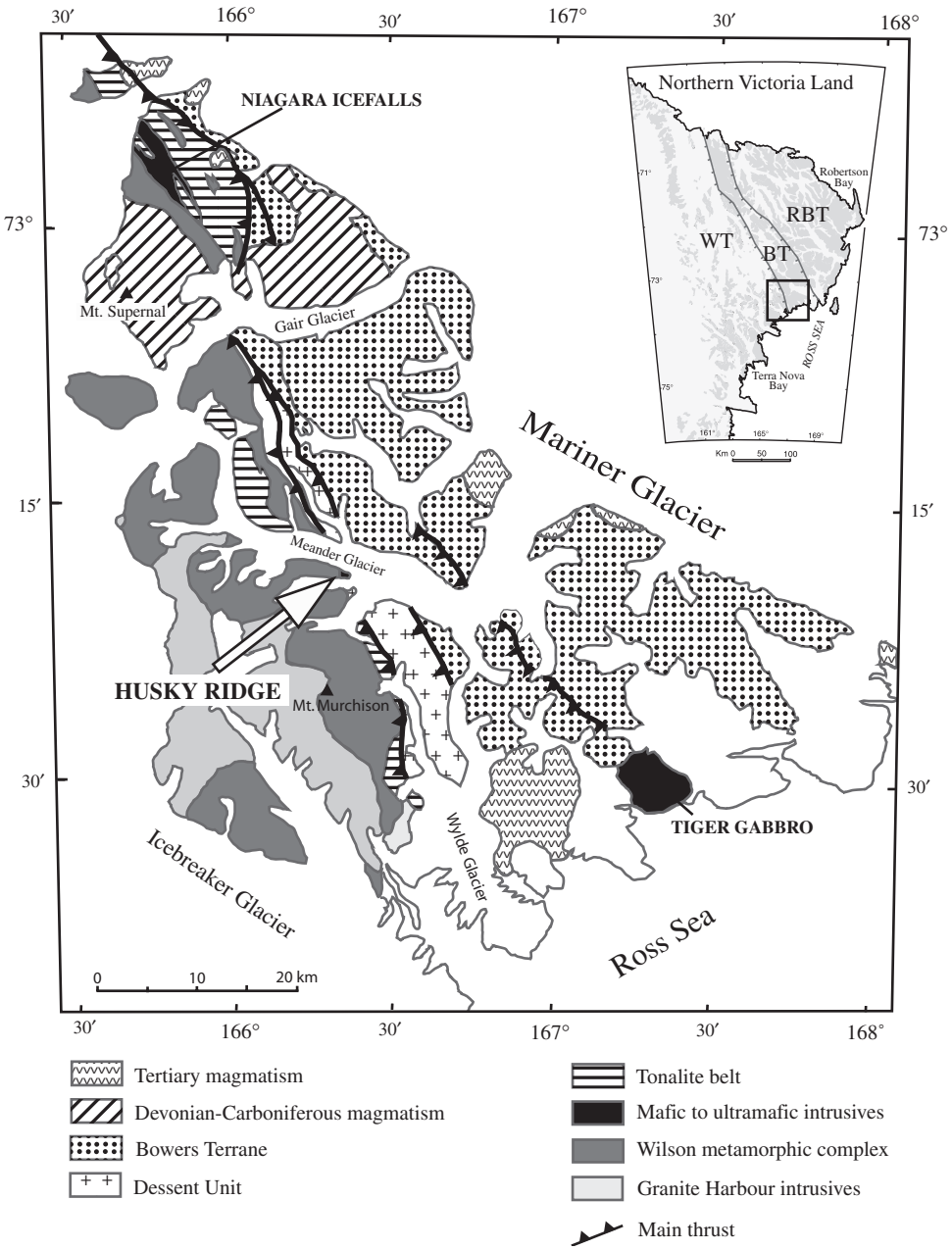

Fig. 1. Geological sketch map of the southern portion of the tectonic boundary between Wilson and Bowers Terranes, northern Victoria Land [redrawn after Musumeci (1999)], showing the location of the Husky Ridge, Tiger gabbro and the Niagara Icefalls gabbroic sequences. Inset shows the location of the map area in northern Victoria Land. WT, Wilson Terrane; BT, Bowers Terrane; RBT, Robertson Bay Terrane.

magmatic products with calc-alkaline affinity found in southern Victoria Land indicate that subduction began at ~540 Ma (Allibone & Wysoczanski, 2002).

In northern Victoria Land (NVL; Fig. 1), three major fault-bounded tectonostratigraphic terranes are identified from west to east: the Wilson, Bowers and Robertson Bay terranes. The origin of these terranes is debated because they are interpreted either as units accreted during the Ross Orogeny (e.g. Tessensohn & Henjes-Kunst, 2005) or as an arc–back-arc–trench system developed during SW-dipping subduction (Federico *et al.*, 2006). There is general consensus, however, in considering the Wilson terrane as representative of the active continental margin of Gondwana at the onset of the subduction. The magmatic products along this continental margin during the Palaeozoic subduction are known as the Granite Harbour

Intrusive series (Gunn & Warren, 1962). In particular, geological and geochronological evidence indicates different phases of emplacement of magma intrusion. In NVL, magmatic products related to the early stages of subduction (e.g. Early Cambrian) are limited to sporadic deformed granitoids with an age between 544 ± 4 Ma and 530 ± 15 Ma (Black & Sheraton, 1990; Rocchi *et al.*, 2004); in addition, rare mafic to ultramafic enclaves dated at 521 ± 4 Ma were found in the Teall Nunatak intrusion (Giacomini *et al.*, 2007). The majority of magmatic products in NVL have ages that cluster around 500 Ma and are mostly granitoids (from granites and granodiorites through tonalites to minor gabbro-diorites) with calcalkaline affinity and variable K_2O enrichment (Di Vincenzo *et al.*, 1997; Rocchi *et al.*, 1998; Dallai *et al.*, 2003). Peraluminous leucogranites and basic melts with shoshonitic affinity were intruded during a late orogenic phase, which probably post-dated the subduction event, at about 480 Ma (Rocchi *et al.*, 1998; Di Vincenzo & Rocchi, 1999). The rare mafic and ultramafic intrusive rocks in NVL are mostly scattered along the suture zone between the Wilson and Bowers terranes (Fig. 1). In particular, three main gabbroic sequences preserve their original intrusive features; namely, the Niagara Icefall, Husky Ridge and Tiger Gabbro sequences. A petrological, geochemical and geochronological study has been recently carried out on the Niagara Icefall mafic–ultramafic intrusion and revealed its boninitic affinity and crystallization age at about 514 Ma (Tribuzio *et al.*, 2007). The petrogenetic affinity and age of the other two gabbroic sequences is poorly defined.

The Husky Ridge (73°20′S, 166°20′E) is located in the middle of the Meander Glacier, *c.* 10 km north of Mt Murchison. The exposed surface of the outcrop is *c.* 2 km in length and about 200 m in width. It mainly consists of amphibolite-facies migmatitic gneisses, locally sillimanite bearing, equilibrated at pressure and temperature conditions of about 5 kbar and 640°C (Castelli *et al.*, 2003). In the eastern sector of the ridge, a body of about 100 m × 50 m of undeformed to weakly deformed amphibole-rich mafic intrusive rocks was found. The host rocks are quartz- and biotite-rich gneisses containing either garnet + white mica or clinopyroxene + amphibole. The occurrence of amphibole-rich mafic intrusive rocks as an undeformed body within amphibolite-facies foliated rocks was similarly observed in the Bregaglia intrusion of the Central Alps (Diethelm, 1985; Tiepolo *et al.*, 2002). The amphibole-rich mafic intrusive rocks consist of large amphibole crystals and minor fine-grained plagioclase-bearing matrix. Layering related to variations in hornblende to plagioclase modal ratios is locally observed (Fig. 2). Plagioclase-rich veinlets (up to 10 cm in width) with subordinate amphibole, quartz and biotite and no fine-grained matrix are locally present. In the easternmost sector of the ridge (*c.* 300 m from the amphibole-rich mafic intrusive rocks), the gneisses contain an intrusive body made of a foliated hornblende- and biotite-bearing tonalite locally displaying modal layering. No contact relations between the amphibole-rich mafic intrusive rocks and tonalites are observed.

PETROGRAPHY

Quartz diorites

According to estimated mineral proportions (Table 1), the Husky Ridge amphibole-rich intrusive rocks are quartz meladiorites to quartz diorites. The large amphibole grains (up to 2 cm) are subhedral with brown cores and green rims (up to 2 mm wide; Fig. 3). The boundary between the two amphiboles is relatively sharp. The green amphibole rim shows intergrowth with plagioclase. Clinopyroxene and minor altered biotite are included in the brown amphibole cores, where no plagioclase occurs. A thin aureole made of green amphibole rims the

Table 1: Petrographic characteristics of selected samples

Sample	Rock type	Matrix %	Mineral proportions	Accessory minerals
TT327	Qtz meladiorite	25·0	Brown Amph (75) + Green Amph (15) + Pl (10)	Bt + Cpx + Qtz + Ox + Tit + Ap
TT329	Qtz meladiorite	25·0	Brown Amph (75) + Green Amph (15) + Pl (10)	Bt + Cpx + Qtz + Ox + Tit + Ap
TT334	Qtz diorite	50·0	Brown Amph (50) + Cpx (15) + Amph (15) + Pl (10) + Qtz (10)	Ox + Ap + Tit + Zrn
TT331	Qtz diorite	70·0	Brown Amph (30) + Cpx (35) + Amph (10) + Pl (20) + Qtz (5)	Ox + Ap + Tit
TT330	Qtz diorite	65·0	Brown Amph (35) + Cpx (20) + Green Amph (25) + Pl (20)	Qtz + Ox + Ap + Tit + Zrn
TT40	Tonalite	—	Pl (37) + Bt (30) + Amph (20) + Qtz (13)	Ox + Ap + Zrn
TT354	Bt gneiss	—	Pl (34) + Bt (25) + Qtz (41)	Ox + Ap + Zrn + All + Gnt + White mica

Amph, amphibole; Pl, plagioclase; Qtz, quartz; Bt, biotite; Ox, oxides; Tit, titanite; Ap, apatite; Zrn, zircon; All, allanite; Gnt, garnet.

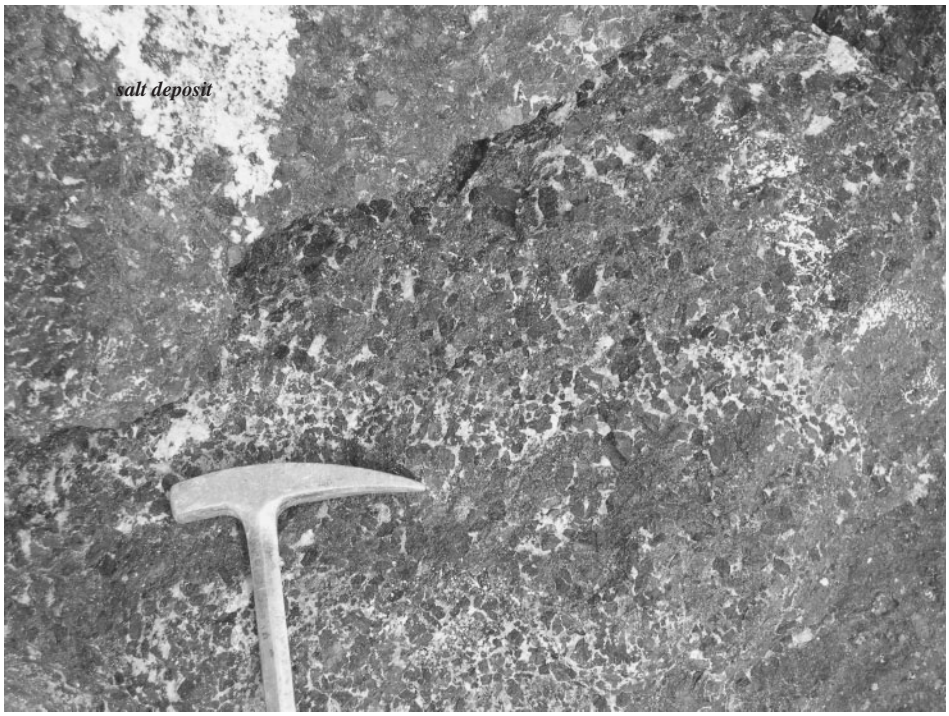

Fig. 2. Typical appearance of the quartz diorites in the field. Large amphibole crystals are dispersed in the minor fine-grained plagioclase-bearing matrix, and the occurrence of plagioclase-rich layers should be noted. The white spots are salt deposits.

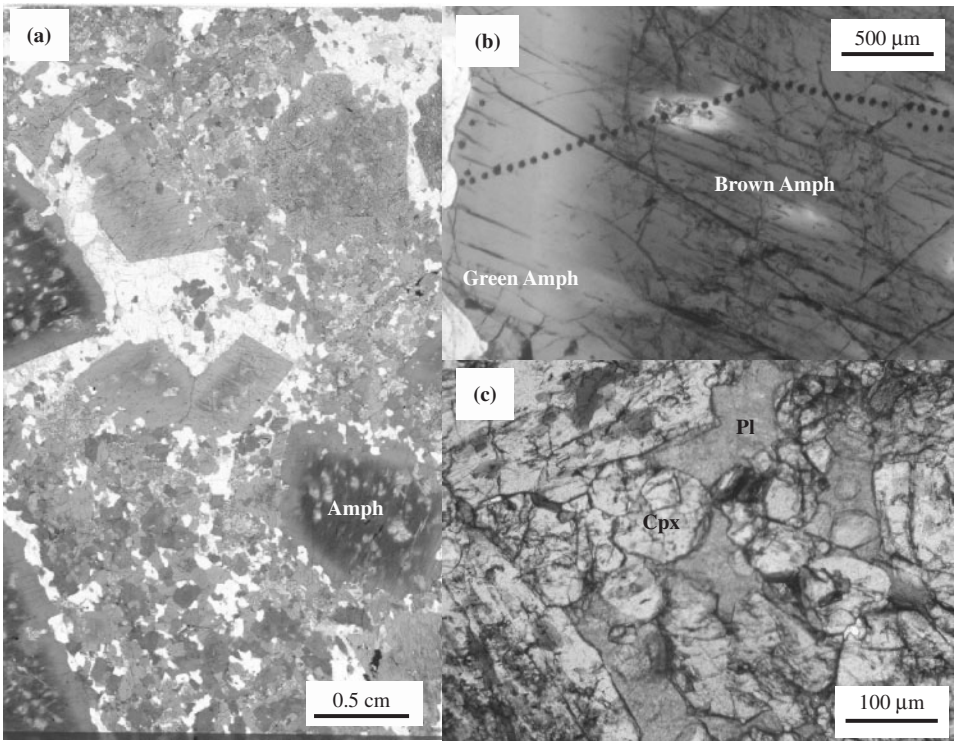

Fig. 3. Photomicrographs (parallel Nicols) of quartz diorites. (a) Overview of the quartz diorite texture, with large zoned amphibole grains dispersed in the fine-grained matrix. (b) Details of a large zoned amphibole grain. Black dots are the laser ablation spots of the compositional traverse. (c) Details of the matrix minerals. Amph, amphibole; Cpx, clinopyroxene; Pl, plagioclase.

clinopyroxene that forms inclusions in the brown amphibole. The fine-grained matrix consists of clinopyroxene, green amphibole, plagioclase and quartz (Fig. 3). Textural relations in the matrix indicate early crystallization of clinopyroxene relative to that of plagioclase and green amphibole. In particular, green amphibole is locally observed to replace clinopyroxene. Plagioclase shows widespread low-temperature alteration. Mineral proportions in the matrix vary from sample to sample, but the mafic/felsic mineral ratio is nearly constant at 1:1. In particular, clinopyroxene within matrix varies from accessory to a major constituent, and quartz (up to 10 vol. %) is modally subordinate to plagioclase. Accessory matrix minerals are titanite, oxide phases, apatite and zircon. Five amphibole-rich mafic rocks, considered to represent the modal variations occurring in this rock-type, were selected for the present study.

Tonalite and host basement rocks

One tonalite and one basement sample were selected for the geochemical and geochronological study, to define the role of the continental crust in the petrogenesis of amphibole-rich intrusive rocks. The selected tonalite has a hypidiomorphic and foliated texture given by the preferential orientation of major minerals (i.e. plagioclase, quartz, amphibole and biotite). Plagioclase and biotite are euhedral to subhedral and are modally predominant over anhedral quartz and amphibole, respectively (Table 1). Accessory minerals in the tonalite are oxide phases, apatite, zircon, allanite and titanite. The selected basement sample has a gneissic texture and mostly consists of quartz, plagioclase and biotite with a well-defined orientation. Accessory garnet and white mica occur in quartz–feldspathic layers. White mica is also locally associated with biotite. Other accessory minerals are oxide phases, apatite, zircon and allanite.

MINERAL COMPOSITION

Analytical procedures

Major element mineral chemistry of clinopyroxene, plagioclase and amphibole from the quartz diorites and the tonalite was determined at CNR–Istituto di Geoscienze e Georisorse, U.O. di Padova, using a Cameca SX 50 electron microprobe and at the Dipartimento di Scienze della Terra Università di Milano using a Jeol Super Probe electron microprobe. Operating conditions were set at 15 kV accelerating voltage and 15 nA beam current on the sample. Trace element mineral composition of amphibole, clinopyroxene, plagioclase and titanite was determined by laser ablation inductively coupled plasma mass spectrometry (LA-ICPMS) at the CNR–Istituto di Geoscienze e Georisorse, U.O. di Pavia. The instrument couples a Nd:YAG laser working at 266 nm with a quadrupole ICP mass spectrometer type DRCe from Perkin Elmer. The laser was operated at 10 Hz with a pulse energy on the sample of 0.01–0.03 mJ. The spot size was set to 30 μm. Data reduction was performed with the 'Glitter' software package (van Achtenbergh *et al.*, 2001) using NIST SRM 612 as the external standard and ^{44}Ca as the internal one. Precision and accuracy, assessed during each analytical run on the BCR-2 USGS reference glass, are up to better than 6% relative.

Quartz diorites

Clinopyroxene

Clinopyroxene included into brown amphibole shows relatively high Mg/(Mg + Fe) ratios (Mg-number = 0·78–0·84) and low contents of Ti (<0·01 a.p.f.u.) and Al (0·02–0·07 a.p.f.u.) (Table 2; Fig. 4). The clinopyroxene in the matrix has slightly lower Mg-number. Trace element determination on clinopyroxene included in brown amphibole (Table 3) reveals a bell-shaped chondrite-normalized REE pattern with the maximum at middle REE (MREE) at about four times Cl (Fig. 5). The La_N/Sm_N ratio ranges between 0·4 and 0·5 and no Eu anomaly is observed. Cr contents in the clinopyroxene included in brown amphibole range between 1130 and 2000 ppm. Its incompatible element pattern shows depletion in Ba, Nb, Pb and Ti relative to the neighbouring elements; conversely, a marked enrichment in Li, Th and U relative to other elements is observed.

Clinopyroxene in the matrix is characterized by a weak LREE enrichment ($La_N/Sm_N = 0·9–2·2$) over HREE, which are almost flat or slightly convex upward at 1·7–6·0 times Cl. No Eu anomaly is observed (Fig. 5). Cr is between 107 and 557 ppm. The incompatible element pattern generally parallels that of clinopyroxene included in brown amphibole. Slightly lower contents of Th and higher contents of Pb are observed. A more marked negative Ti anomaly is also detected.

Brown amphibole

Brown amphibole has a relatively homogeneous major and trace element composition (Tables 4 and 6). It is characterized by Ti contents up to 0·18 a.p.f.u. and Mg-number of ~0·70 (Fig. 6). Al_{Tot} is up to 1·87 a.p.f.u., and the alkali content (Na + K) ranges from 0·37 to 0·57 a.p.f.u. The chondrite-normalized REE pattern varies from flat to slightly convex downward ($La_N/Sm_N = 0·4–0·7$), with MREE at about 20 times Cl (Fig. 5). No significant Eu anomaly is observed. The highest Cr and Ni contents (up to 1010 and 442 ppm, respectively) are from brown amphibole in matrix-poor samples. The incompatible element pattern reveals a strong depletion of Rb relative to Ba, which is at the same level as LREE (Fig. 5). Nb and Ta are slightly depleted relative to LREE, whereas both Pb and Zr–Hf are significantly depleted relative to the neighbouring HREE. Th contents are comparable

with those of LREE, whereas U is significantly enriched (U/Th = 0·95–2·3). Li and B contents are variable, with values up to 18 ppm and 11·4 ppm, respectively.

Green amphibole

The green amphiboles in the matrix and the green amphibole rimming brown amphibole have similar major and trace element compositions (Tables 5 and 6). Compared with brown amphibole, green amphibole shows lower Al_{Tot}, Ti and $(Na + K)_A$ contents, coupled with slightly higher Mg-number (up to 0·74; Fig. 6). The lowest Al_{Tot} and Ti contents of green amphibole are 1·07 and 0·03 a.p.f.u., respectively. The chondrite-normalized REE pattern of green amphibole is characterized by LREE enrichment over HREE ($La_N/Sm_N = 1·0–2·5$). LREE concentrations in green amphibole are about twice those in brown amphibole (Fig. 5). The incompatible trace element pattern reveals lower Sr, Pb and U contents than in brown amphiboles and significantly higher concentrations of Nb and Ta. Cr contents are comparable with or slightly lower than those in brown amphibole (374–807 ppm), whereas Ni values are always slightly lower (196–300 ppm). Li and B contents are similar to those observed in brown amphibole.

Trace element profile across amphibole

A core-to-rim trace element profile was performed across one well-preserved amphibole grain from sample TT334 to constrain the chemical transition between brown and green amphibole (Fig. 7). A total of 39 analyses were carried out with a spot size of 40 μm and at intervals of about 40–50 μm (details are given in Electronic Appendix 1, which is available for downloading at http://www.petrology.oxfordjournals.ac.uk).

Transition metals (e.g. Cr, Mg, Zn, Ni, Co) and some LILE (Ba and Rb) show minor variations within and between the two types of amphibole. The REE concentrations are different but homogeneous within the green and brown amphibole domains. The transition between these two domains is relatively narrow (about 200 μm) and intermediate concentrations of REE are observed. The green amphibole is depleted in HREE relative to the brown amphibole by a factor of about two. Conversely, the LREE content in the green amphibole is twice that in the brown amphibole. Ti, Nb and Ta contents differ the

Table 2: Representative major element composition (wt %) of clinopyroxene from quartz diorites

Sample:	TT330	TT330	TT330	TT330	TT328	TT328	TT327	TT327	TT329	TT329	TT329	TT331	TT331	TT331	TT331	TT334	TT334	TT334
Position:	in Amph	in Amph	in Amph	in Amph	in Amph	in Amph	in Amph	in Amph	matrix	matrix	matrix	matrix	matrix	matrix	matrix	matrix	matrix	matrix
SiO_2	54.14	53.96	54.28	54.57	53.93	54.52	54.57	54.58	53.74	53.71	53.99	53.77	54.04	53.77	53.77	54.12	54.06	53.83
TiO_2	0.22	0.21	0.16	0.00	0.12	0.14	0.16	0.09	0.23	0.10	0.13	0.06	0.07	0.16	0.09	0.05	0.00	0.11
Al_2O_3	1.48	1.38	1.29	0.48	1.34	0.95	1.09	0.69	1.58	1.19	0.88	1.33	1.11	1.91	1.47	0.87	1.26	1.32
Cr_2O_3	0.18	0.17	0.14	0.04	0.04	0.14	0.26	0.02	0.11	0.17	0.10	0.01	0.03	0.05	0.00	0.00	0.00	0.04
FeO_T	5.15	5.72	5.47	6.37	6.76	5.96	5.66	5.64	6.57	6.45	6.23	6.87	6.23	6.99	6.75	6.59	6.81	6.64
MnO	0.13	0.17	0.17	0.27	0.21	0.24	0.16	0.22	0.20	0.27	0.22	0.22	0.18	0.16	0.17	0.29	0.31	0.15
MgO	15.13	14.69	15.06	14.24	14.02	14.48	14.91	14.75	14.94	14.49	14.64	14.27	14.47	14.81	14.38	14.33	13.99	14.22
CaO	24.18	23.98	23.59	24.35	23.92	24.08	23.93	24.45	23.10	24.22	24.43	24.06	24.57	22.61	23.91	24.35	24.16	24.06
Na_2O	0.32	0.38	0.33	0.28	0.42	0.33	0.30	0.29	0.39	0.27	0.29	0.30	0.27	0.45	0.44	0.34	0.37	0.42
Total	100.9	100.7	100.5	100.6	100.8	100.8	101.0	100.7	100.9	100.9	100.9	100.9	101.0	100.9	101.0	100.9	101.0	100.8
Si	1.97	1.98	1.99	2.01	1.98	1.99	1.99	2.00	1.97	1.97	1.98	1.97	1.98	1.97	1.97	1.98	1.98	1.98
Al	0.06	0.06	0.06	0.02	0.06	0.04	0.05	0.03	0.07	0.05	0.04	0.06	0.05	0.08	0.06	0.04	0.05	0.06
Fe^{3+}	0.00	0.00	0.00	0.00	0.00	0.00	0.00	0.00	0.01	0.02	0.02	0.01	0.01	0.01	0.03	0.01	0.00	0.01
Ti	0.01	0.01	0.00	0.00	0.00	0.00	0.00	0.00	0.01	0.00	0.00	0.00	0.00	0.00	0.00	0.00	0.00	0.00
Cr	0.01	0.00	0.00	0.00	0.00	0.00	0.01	0.00	0.00	0.00	0.00	0.00	0.00	0.00	0.00	0.00	0.00	0.00
Mg	0.82	0.80	0.82	0.78	0.77	0.79	0.81	0.80	0.81	0.79	0.80	0.78	0.79	0.81	0.78	0.78	0.77	0.78
Fe^{2+}	0.16	0.18	0.17	0.20	0.21	0.18	0.17	0.17	0.19	0.18	0.17	0.20	0.18	0.20	0.18	0.19	0.20	0.19
Mn	0.00	0.01	0.01	0.01	0.01	0.01	0.00	0.01	0.01	0.01	0.01	0.01	0.01	0.00	0.01	0.01	0.01	0.00
Ca	0.94	0.94	0.92	0.96	0.94	0.94	0.93	0.96	0.91	0.95	0.96	0.95	0.96	0.89	0.94	0.96	0.95	0.95
Na	0.02	0.03	0.02	0.02	0.03	0.02	0.02	0.02	0.03	0.02	0.02	0.02	0.02	0.03	0.03	0.02	0.03	0.03
Mg-no.	0.84	0.82	0.83	0.80	0.79	0.81	0.82	0.82	0.80	0.80	0.81	0.79	0.81	0.79	0.79	0.79	0.79	0.79

in Amph, included in brown amphibole; matrix, within the matrix; Mg-number = Mg/(Mg + Fe).

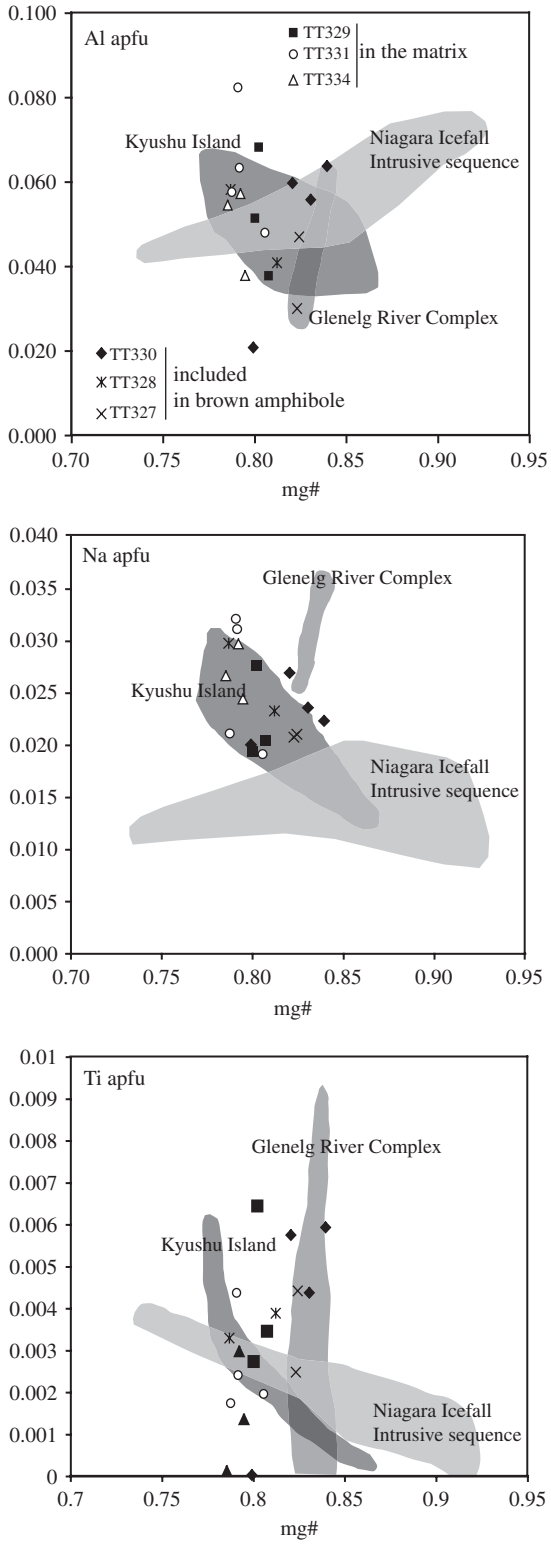

Fig. 4. Compositional variations in clinopyroxene. For comparison the fields for clinopyroxene from diorites of Kyushu (Kamei *et al.*, 2004), from quartz melagabbros of the Glenelg River Complex (Kemp, 2004) and from mafic–ultramafic intrusive rocks of the Niagara Icefall Complex (Tribuzio *et al.*, 2007) are shown.

most (by a factor of about five) between the two types of amphibole. Ti confirms the presence of a narrow (about 200 μm) interface region with values intermediate to those of brown and green amphiboles. Ti contents in brown and green amphiboles are almost constant. Zr and Nb increase slightly from the core to the rim of brown amphiboles. Values are almost constant across the interface and then quickly increase, becoming nearly constant for the whole width of the green amphibole. Th, U and LILE (Li and B) concentrations are highly scattered, and no significant variations can be detected across the amphibole grain. Pb contents in green amphibole are depleted with respect to those in brown amphibole, but are almost constant within the two amphibole types. To sum up, the element distribution across the amphibole grain reveals that Mg, Cr and Ba show no systematic variations between the two types of amphibole, whereas the concentrations of elements such as REE, Ti and Nb differ significantly between brown and green amphibole. In particular, the latter elements show marked, sudden variations within a zone of a few hundred microns. It should be noted that none of the analysed elements show constant, steady variations in concentrations from the brown core to the green rim.

Plagioclase and titanite

The An content of plagioclase ranges from 35 to 46 mol % (Tables 7 and 8). The chondrite-normalized element pattern is characterized by a marked fractionation between LREE and MREE (La is about 10 times Cl, and Sm less than 0·5 times Cl; Fig. 8). Slightly lower REE values are observed in plagioclase from samples with low An contents. If plagioclase of quartz diorites from the Husky Ridge is compared with that formed from MOR-type melts, more than one order of magnitude of LREE enrichment is observed (Fig. 8). The concentrations of Sr and Ba in analysed plagioclase show a narrow range of variation, with values of 665–744 ppm and 118–131 ppm, respectively. Ti is between 11·4 and 21·3 ppm; Li is below 0·35 ppm, and B ranges between 4·5 and 9·5 ppm.

The trace element composition of three titanite crystals from sample TT329 was determined (Table 8). The REE pattern has a marked enrichment in LREE (up to 3000–7200 times Cl) over HREE (at about 400–650 times Cl) and a weak negative Eu anomaly. One of the crystals does not show the negative Eu anomaly, and this feature is coupled with the highest LREE, Th and U contents. The incompatible element pattern reveals U and Th values comparable with those of LREE. Zr–Hf and Nb–Ta are slightly depleted relative to the neighbouring elements. Sr and Pb contents are less than 10 times Cl chondrite.

Table 3: Trace element composition of clinopyroxene (ppm) from quartz diorites

Sample:	TT330	TT330	TT330	TT327	TT327	TT334	TT334	TT334	TT331	TT331	TT331	TT331	TT331	TT331	TT331	TT331
Position:	in amph	in amph	in amph	in amph	in amph	matrix	matrix	matrix	matrix	matrix	matrix	matrix	matrix	matrix	matrix	matrix
Li	20.8	18.8	27.5	18.7	14.7	24.8	24.8	26.8	23.4	23.2	26.5	23.0	27.2	25.2	25.6	24.3
B	—	—	—	—	—	2.91	4.09	2.19	<1.29	3.34	2.27	1.80	2.52	2.18	4.08	2.83
Na	—	—	—	—	—	4292	4619	4210	4580	4598	5004	4789	5067	5210	5144	4976
Sc	84.6	82.8	79.6	91.3	81.3	46.7	50.6	47.5	64.3	60.3	63.5	62.1	63.8	62.8	61.5	68.1
Ti	1566	1534	1537	1038	999	243	206	262	463	464	547	563	669	633	521	546
V	249.5	253.5	247.1	214.4	217.2	69.0	72.6	71.9	129	126	129	140	131	131	118	146
Cr	1150	1412	1666	1992	1128	244	271	194	180	151	130	147	119	107	130	125
Co	43.0	43.1	42.9	48.1	48.3	30.4	32.0	31.7	34.4	34.4	33.0	34.4	32.8	32.4	33.4	33.5
Ni	—	—	—	—	—	89.8	89.1	84.0	108	111	104	111	105	101	108	106
Zn	—	—	—	—	—	55.2	54.4	42.5	42.8	44.5	41.5	41.0	42.0	43.1	43.4	43.2
Rb	<0.090	<0.093	<0.097	<0.059	0.129	0.150	0.048	<0.0307	<0.033	<0.031	<0.037	0.031	<0.037	<0.029	<0.041	<0.041
Sr	23.6	24.1	22.2	24.9	25.5	21.0	27.0	21.0	21.5	19.8	20.5	20.7	23.5	21.4	20.8	21.0
Y	4.19	4.15	4.66	3.46	4.34	2.52	2.71	2.39	4.25	4.17	4.70	4.47	5.57	5.19	4.54	4.63
Zr	7.74	6.85	9.52	6.15	8.76	6.35	5.56	5.60	7.29	7.47	8.38	8.82	10.6	11.3	8.37	9.86
Nb	0.137	0.126	0.069	0.035	0.063	0.029	<0.038	0.024	<0.0172	<0.0109	0.027	0.022	0.022	<0.0148	<0.0193	0.024
Ba	0.534	0.840	0.539	0.683	0.735	0.151	0.182	0.156	<0.081	<0.072	<0.118	<0.056	<0.096	<0.069	<0.109	<0.105
La	0.50	0.40	0.61	0.50	0.44	1.58	1.77	1.48	1.37	1.37	1.69	1.34	1.65	1.65	1.58	1.66
Ce	1.75	1.76	1.91	1.69	1.41	4.90	4.84	4.79	4.31	4.12	5.24	4.26	5.83	5.95	5.40	5.34
Pr	0.310	0.346	0.373	0.303	0.318	0.625	0.620	0.710	0.664	0.677	0.787	0.659	0.900	0.854	0.755	0.832
Nd	2.06	1.93	2.33	2.05	2.02	2.58	2.25	2.98	3.35	2.86	3.17	3.32	3.83	3.45	3.15	3.63
Sm	0.641	0.608	0.712	0.587	0.588	0.594	0.674	0.409	0.679	0.791	0.915	0.767	0.990	1.11	0.980	0.860
Eu	0.234	0.224	0.255	0.197	0.198	0.188	0.169	0.114	0.264	0.240	0.263	0.208	0.227	0.217	0.201	0.224
Gd	0.935	0.792	0.854	0.814	0.908	0.407	0.612	0.440	0.646	1.07	0.923	0.995	0.840	0.820	0.780	0.955
Tb	0.154	0.162	0.154	0.124	0.180	0.070	0.073	0.099	0.168	<0.149	0.160	0.113	0.184	0.178	0.154	0.153
Dy	0.975	0.985	1.042	0.889	0.953	0.504	0.491	0.526	0.981	0.966	1.01	1.046	1.084	1.053	0.947	1.150
Ho	0.206	0.208	0.234	0.165	0.231	0.079	0.111	0.108	0.156	0.196	0.175	0.220	0.206	0.234	0.201	0.219
Er	0.536	0.551	0.632	0.409	0.608	0.234	0.300	0.249	0.470	0.560	0.549	0.519	0.614	0.472	0.548	0.482
Tm	0.063	0.075	0.072	0.066	0.071	0.054	0.065	0.043	0.065	<0.1	0.087	0.097	0.081	0.076	0.073	0.085
Yb	0.377	0.380	0.532	0.383	0.528	0.276	0.307	0.440	0.557	0.404	0.584	0.729	0.750	0.414	0.547	0.776
Lu	0.074	0.063	0.063	0.063	0.066	0.051	0.059	0.062	0.068	0.066	0.103	0.070	0.110	0.109	0.095	0.112
Hf	0.435	0.387	0.576	0.406	0.457	0.364	0.291	0.328	0.425	0.395	0.524	0.427	0.603	0.573	0.485	0.600
Ta	0.006	0.009	<0.0047	<0.0038	<0.0030	0.005	0.021	0.012	<0.0172	<0.0134	<0.0103	0.016	<0.0119	<0.0128	<0.02	0.022
Pb	0.357	0.432	0.346	0.775	0.738	0.847	1.013	0.850	0.796	1.096	0.931	0.797	0.693	0.673	0.954	1.335
Th	0.288	0.343	0.220	0.141	0.147	0.086	0.041	0.061	0.027	0.037	0.069	0.037	0.039	0.059	0.048	0.067
U	0.058	0.068	0.021	0.045	0.079	0.055	0.026	0.031	0.014	0.011	0.024	0.022	0.025	0.037	0.030	0.027
La_N/Sm_N	0.48	0.40	0.51	0.52	0.45	1.62	1.59	2.20	1.22	1.05	1.12	1.06	1.01	0.90	0.98	1.17

in amph, included in brown amphibole; matrix, within matrix minerals.

Tonalite

Amphibole from the tonalite sample (Tables 6 and 9) has lower Ti (0·13–0·14 a.p.f.u.) and higher Al_{tot} (1·89–2·14 a.p.f.u.) than amphibole from quartz diorites (Fig. 6). Its low Mg-number (0·50–0·53) is noteworthy. The REE pattern (Fig. 5) differs from that of brown and green amphiboles in the quartz diorites. It is characterized by a strong depletion of LREE ($La_N/Sm_N = 0·17–0·21$) relative to MREE and HREE, which are about 60 times Cl. Eu shows a marked negative anomaly relative to the neighbouring REE. The incompatible element pattern reveals higher Rb and significantly lower Th and U

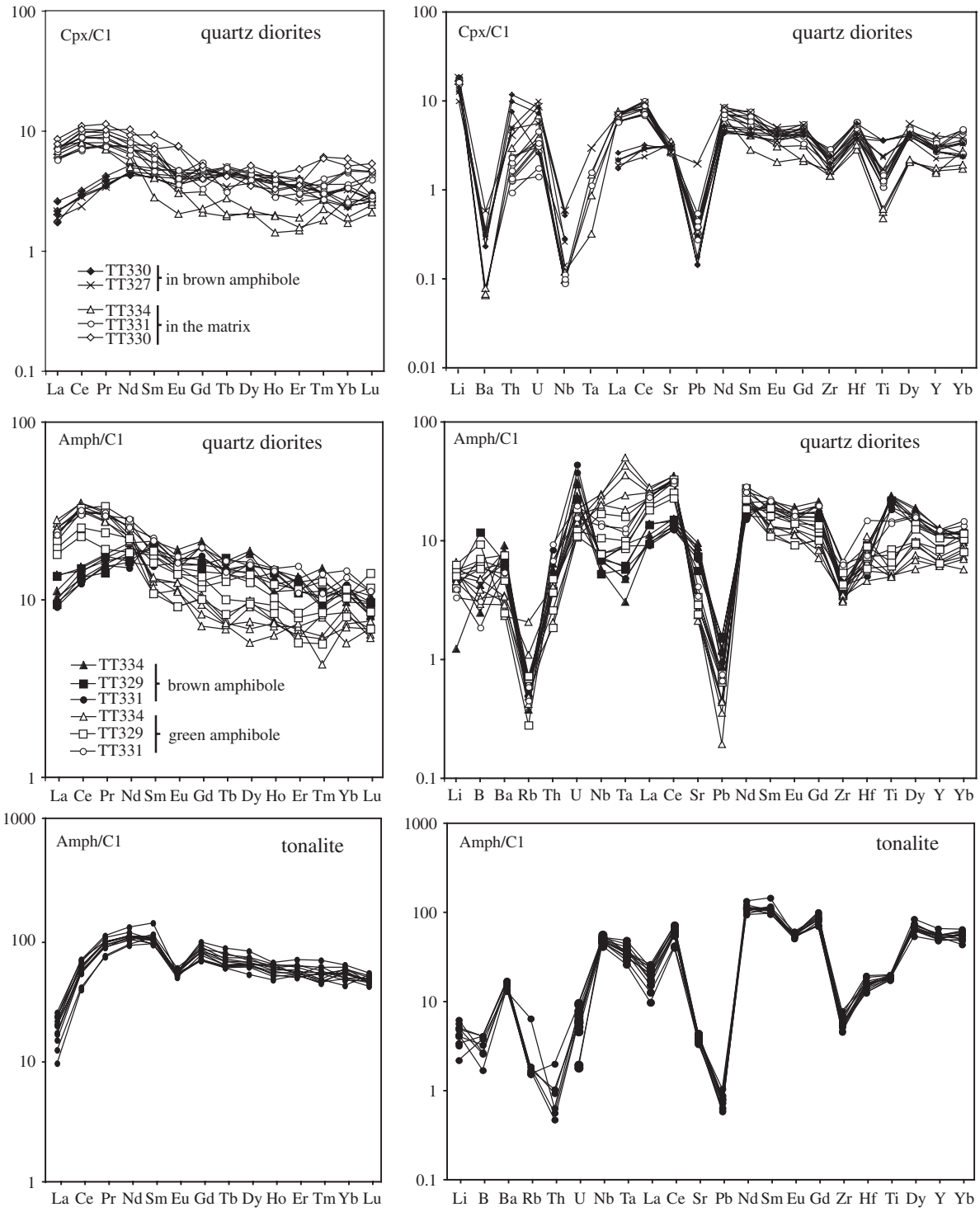

Fig. 5. Chondrite-normalized rare earth element and incompatible element patterns for amphibole and clinopyroxene from quartz diorites and tonalite. Normalization values are from Anders & Ebihara (1982).

contents than the two types of amphibole in quartz diorites. Zr, Hf, Nb, Ta and LREE contents are almost comparable with those of green amphibole in quartz diorites. Cr contents are lower than in quartz diorites, with values in the 113–280 ppm range. Li is below 7·5 ppm, and B ranges between 1·6 and 3·98 ppm.

Plagioclase from the tonalite sample has An contents of 42–48 mol %. The REE pattern reveals generally higher

Table 4: Representative major element composition (wt %) of brown amphibole in quartz diorites

Sample:	TT329	TT329	TT329	TT329	TT329	TT329	TT329	TT329	TT334	TT334	TT334	TT331	TT331	TT331	TT331	TT331
SiO_2	45.90	48.79	45.94	46.18	46.06	46.02	46.16	46.13	45.44	46.25	45.55	46.84	47.04	49.24	48.69	48.63
TiO_2	1.54	0.64	1.55	1.57	1.42	1.52	1.57	1.43	1.34	1.58	1.65	1.27	1.22	1.04	1.07	0.97
Al_2O_3	10.42	7.85	10.81	10.90	10.94	10.72	10.73	10.88	10.78	10.85	10.72	10.93	10.78	7.84	8.14	8.02
Cr_2O_3	0.06	0.09	0.07	0.09	0.08	0.16	0.10	0.08	0.06	0.17	0.03	0.00	0.02	0.13	0.09	0.03
FeO_T	11.33	11.51	10.92	10.93	10.68	10.27	10.14	10.23	10.73	10.58	10.61	10.30	10.44	10.58	10.65	10.83
MnO	0.08	0.15	0.19	0.26	0.23	0.19	0.18	0.19	0.15	0.27	0.19	0.15	0.22	0.13	0.15	0.24
MgO	13.60	14.64	14.10	14.04	14.11	14.26	14.66	14.30	14.04	14.11	14.23	14.68	14.62	15.44	15.05	15.08
CaO	12.40	12.16	12.20	12.35	12.21	12.27	12.42	12.18	11.92	12.18	12.11	12.50	12.10	12.41	12.23	12.34
Na_2O	1.46	1.05	1.63	1.41	1.68	1.54	1.45	1.59	1.83	1.69	1.71	1.64	1.76	1.06	1.12	1.26
K_2O	0.46	0.53	0.32	0.32	0.25	0.43	0.45	0.47	0.26	0.29	0.23	0.20	0.22	0.50	0.28	0.43
Total	97.26	97.41	97.72	98.06	97.66	97.38	97.86	97.49	96.55	97.97	97.03	98.52	98.40	98.37	97.47	97.84
Si	6.71	7.08	6.66	6.67	6.68	6.68	6.67	6.69	6.67	6.68	6.65	6.71	6.74	7.05	7.03	7.02
Ti	0.17	0.07	0.17	0.17	0.15	0.17	0.17	0.16	0.15	0.17	0.18	0.14	0.13	0.11	0.12	0.11
Al	1.79	1.34	1.85	1.86	1.87	1.83	1.83	1.86	1.86	1.85	1.84	1.84	1.82	1.32	1.38	1.36
Cr	0.01	0.01	0.01	0.01	0.01	0.02	0.01	0.01	0.01	0.02	0.00	0.00	0.00	0.02	0.01	0.00
Fe	1.38	1.40	1.32	1.32	1.29	1.25	1.23	1.24	1.32	1.28	1.30	1.23	1.25	1.27	1.29	1.31
Mn	0.01	0.02	0.02	0.03	0.03	0.02	0.02	0.02	0.02	0.03	0.02	0.02	0.03	0.02	0.02	0.03
Mg	2.96	3.16	3.05	3.02	3.05	3.08	3.15	3.09	3.07	3.04	3.09	3.13	3.12	3.29	3.24	3.24
Ca	1.94	1.89	1.90	1.91	1.90	1.91	1.92	1.89	1.87	1.88	1.89	1.92	1.86	1.90	1.89	1.91
Na	0.41	0.29	0.46	0.40	0.47	0.43	0.41	0.45	0.52	0.47	0.48	0.46	0.49	0.29	0.31	0.35
K	0.09	0.10	0.06	0.06	0.05	0.08	0.08	0.09	0.05	0.05	0.04	0.04	0.04	0.09	0.05	0.08
Mg/(Mg + Fe)	0.68	0.69	0.70	0.70	0.70	0.71	0.72	0.71	0.70	0.70	0.70	0.72	0.71	0.72	0.72	0.71
Na + K	0.50	0.39	0.52	0.45	0.52	0.51	0.49	0.53	0.57	0.53	0.53	0.49	0.53	0.39	0.37	0.43

Cations are normalized to 23 oxygens.

values than in plagioclase from quartz diorites and a less marked LREE/MREE fractionation (Fig. 8). Sr concentration is 641 ppm, whereas that of Ba and Pb is 61 and 12·5 ppm, respectively. Li is <0·2 ppm and B is at 3·81 ppm.

U–PB ZIRCON GEOCHRONOLOGY AND TRACE ELEMENT COMPOSITION

Analytical methods

Zircons for U–Pb geochronology were separated from three quartz diorites, the tonalite and the Bt-gneiss using standard magnetic techniques and heavy liquids. Because of the paucity of zircons within quartz diorites, the three samples were combined (TT328, TT331 and TT327). Grains without fractures and as free from inclusions as possible were hand picked, embedded in epoxy resin and polished to ¼ μm using diamond paste. Prior to age determination all zircon grains were investigated by cathodoluminescence (CL) to highlight zoning and possible inherited cores. *In situ* U–Pb geochronology was carried out by excimer laser ablation (ELA)-ICPMS at CNR–Istituto di Geoscienze e Georisorse (IGG), Unità di Pavia. The laser ablation instrument couples an ArF excimer laser microprobe at 193 nm (Geolas200Q-Microlas) with a ThermoFinnigan Element I sector field high-resolution ICPMS system. The analytical method is basically as described by Tiepolo (2003). Instrumental and laser-induced U/Pb fractionations were corrected using the 1065 Ma 91500 zircon (Widenbeck *et al.*, 1995) as an external standard. The same integration intervals and spot size were used on both the external standard and unknowns. During each analytical run reference zircon 02123 (295 Ma; Ketchum *et al.*, 2001) was analysed together with unknowns for quality control: its mean concordia age was 297 ± 10 Ma (see Electronic Appendix 2). The spot size was set to 20 or 10 μm and laser fluence to 12 J/cm^2. Data reduction was carried out using the 'Glitter' software package (van Achterbergh *et al.*, 2001). During each analytical run the reproducibility on the standards was propagated to all determinations according to the equation of Horstwood *et al.* (2003). After this operation, analyses are considered accurate within quoted errors. Concordia ages were determined and concordia plots were constructed using the Isoplot/EX 3.0 software (Ludwig, 2000). All errors on

Table 5: Representative major element composition (wt %) of green amphibole in quartz diorites

Sample:	TT329	TT329	TT329	TT329	TT329	TT329	TT329	TT334	TT334	TT334	TT334	TT334	TT334	TT334	TT334	TT334	TT331	TT331	TT331	TT331	TT331	TT331	TT331	TT331	TT331
SiO_2	49.40	50.04	50.07	49.85	50.42	50.58	49.76	51.09	50.96	51.32	51.02	51.33	51.15	51.38	49.95	49.65	48.97	48.51	49.31	48.35	49.85	48.54	50.67	50.44	49.74
TiO_2	0.68	0.54	0.57	0.65	0.66	0.56	0.68	0.30	0.41	0.30	0.30	0.32	0.25	0.32	0.34	0.44	0.88	0.94	0.95	0.99	0.88	1.05	0.69	0.80	0.79
Al_2O_3	7.03	7.05	7.24	7.51	7.09	6.55	6.58	6.45	6.58	6.35	6.39	6.44	6.75	6.38	6.50	7.45	8.31	8.26	8.06	8.27	7.26	8.04	6.79	6.84	6.96
Cr_2O_3	0.10	0.07	0.01	0.07	0.00	0.10	0.10	0.04	0.08	0.04	0.19	0.01	0.09	0.11	0.20	0.12	0.00	0.10	0.08	0.03	0.03	0.00	0.05	0.09	0.05
FeO_T	11.55	11.40	10.20	10.26	9.73	11.42	11.07	10.51	11.04	10.06	10.72	10.39	10.24	10.61	10.43	11.07	10.82	10.97	10.61	11.29	9.98	10.57	10.87	10.87	10.35
MnO	0.21	0.26	0.15	0.14	0.22	0.17	0.22	0.21	0.21	0.17	0.13	0.21	0.13	0.16	0.20	0.21	0.19	0.22	0.16	0.18	0.15	0.18	0.12	0.13	0.26
MgO	14.89	14.63	15.92	15.83	15.90	15.42	15.65	16.12	16.20	16.53	16.10	16.18	15.81	15.90	15.70	15.21	14.99	14.75	14.94	14.83	15.65	15.13	15.70	15.54	15.95
CaO	12.16	12.29	12.23	12.38	12.18	12.30	12.50	12.21	12.25	11.91	12.08	12.50	12.26	12.25	12.41	12.41	12.59	12.27	12.48	12.43	12.52	12.43	12.38	12.54	12.30
Na_2O	0.95	0.86	0.93	1.08	0.96	0.88	0.81	0.85	1.10	1.00	0.88	0.89	0.91	0.93	0.99	0.94	1.01	1.11	1.23	0.94	0.88	1.04	0.89	0.82	0.84
K_2O	0.52	0.49	0.45	0.51	0.41	0.49	0.44	0.41	0.36	0.18	0.32	0.32	0.40	0.38	0.39	0.47	0.56	0.55	0.35	0.73	0.64	0.71	0.42	0.52	0.53
Total	97.50	97.64	97.77	98.27	97.56	98.47	97.82	98.19	99.18	97.84	98.14	98.60	97.99	98.42	97.11	97.96	98.33	97.68	98.17	98.05	97.84	97.68	98.58	98.59	97.77
Si	7.16	7.22	7.18	7.12	7.22	7.24	7.17	7.29	7.22	7.31	7.29	7.29	7.30	7.31	7.23	7.14	7.02	7.01	7.07	6.98	7.15	7.01	7.22	7.20	7.15
Ti	0.07	0.06	0.06	0.07	0.07	0.06	0.07	0.03	0.04	0.03	0.03	0.03	0.03	0.03	0.04	0.05	0.10	0.10	0.10	0.11	0.10	0.11	0.07	0.09	0.09
Al	1.20	1.20	1.22	1.26	1.20	1.10	1.12	1.08	1.10	1.07	1.08	1.08	1.13	1.07	1.11	1.26	1.40	1.41	1.36	1.41	1.23	1.37	1.14	1.15	1.18
Cr	0.01	0.01	0.00	0.01	0.00	0.01	0.01	0.00	0.01	0.00	0.02	0.00	0.01	0.01	0.02	0.01	0.00	0.01	0.01	0.00	0.00	0.00	0.01	0.01	0.01
Fe	1.40	1.38	1.22	1.23	1.16	1.37	1.33	1.25	1.31	1.20	1.28	1.23	1.22	1.26	1.26	1.33	1.30	1.33	1.27	1.36	1.20	1.28	1.30	1.30	1.24
Mn	0.03	0.03	0.02	0.02	0.03	0.02	0.03	0.03	0.02	0.02	0.02	0.03	0.02	0.02	0.02	0.03	0.02	0.03	0.02	0.02	0.02	0.02	0.01	0.02	0.03
Mg	3.22	3.15	3.40	3.37	3.39	3.29	3.36	3.43	3.42	3.51	3.42	3.42	3.36	3.37	3.38	3.26	3.20	3.18	3.19	3.19	3.34	3.26	3.33	3.30	3.41
Ca	1.89	1.90	1.88	1.90	1.87	1.89	1.93	1.87	1.86	1.82	1.85	1.90	1.87	1.87	1.92	1.91	1.94	1.90	1.92	1.92	1.92	1.92	1.89	1.92	1.89
Na	0.27	0.24	0.26	0.30	0.27	0.24	0.23	0.23	0.30	0.28	0.24	0.24	0.25	0.26	0.28	0.26	0.28	0.31	0.34	0.26	0.25	0.29	0.25	0.23	0.24
K	0.10	0.09	0.08	0.09	0.07	0.09	0.08	0.07	0.06	0.03	0.06	0.06	0.07	0.07	0.07	0.09	0.10	0.10	0.06	0.13	0.12	0.13	0.08	0.10	0.10
$Mg/(Mg+Fe)$	0.70	0.70	0.74	0.73	0.74	0.71	0.72	0.73	0.72	0.75	0.73	0.73	0.73	0.73	0.73	0.71	0.71	0.71	0.71	0.70	0.74	0.72	0.72	0.72	0.73
$Na+K$	0.36	0.33	0.34	0.39	0.34	0.33	0.31	0.31	0.37	0.31	0.30	0.30	0.32	0.32	0.35	0.35	0.38	0.41	0.41	0.40	0.36	0.42	0.32	0.32	0.33

Cations are normalized to 23 oxygens.

Table 6: Trace element composition of amphiboles (ppm)

Rock type:	Qtz diorite Brown amphibole								Qtz diorite Green amphibole			
Sample:	TT329	TT329	TT334	TT334	TT334	TT334	TT331	TT331	TT329	TT329	TT329	TT329
Li	7.18	8.33	9.32	8.33	7.83	8.55	6.63	7.5	8.12	9.35	5.94	7.52
B	11.5	6.69	<0.82	2.41	4.12	4.65	5.64	4.43	6.08	9.09	6.89	5.67
Na	20762	19241	19077	20736	20743	21019	22606	21312	11668	13869	13116	13616
Sc	65.0	61.1	66.1	70.9	75.7	81.3	57.4	56.7	44.2	44.7	43.7	42.9
Ti	9479	9339	10094	10321	10146	10124	8249	7915	2647	2867	3678	3265
V	505	460	523	509	491	514	376	353	172	195	233	214
Cr	573	591	675	750	702	647	208	194	546	807	583	583
Co	61.3	58.8	67.6	63.7	61.4	62.8	68.3	62.6	48.9	49.7	56.6	59.5
Ni	422	402	429	427	396	394	327	299	196	213	267	283
Zn	70.5	77.5	69.0	64.8	58.4	56.7	61.4	64.8	101	114	71.4	77.2
Rb	1.371	1.406	0.862	1.179	1.202	1.347	1.126	1.079	1.579	0.639	1.642	1.66
Sr	57.3	43.3	68.7	73.8	63.0	68.2	59.6	53.8	18.6	22.4	22.4	26.1
Y	16.7	17.4	17.7	19.3	19.4	19.7	16.3	17.2	16.4	13.4	13.1	10.0
Zr	14.8	13.6	14.7	17.4	17.2	17.1	16.2	16.6	16.2	22.9	16.8	21.1
Nb	1.28	1.691	1.40	1.66	1.77	1.68	1.669	1.641	4.12	2.58	1.904	1.884
Cs	0.018	0.035	<0.018	0.05	0.01	<0.008	<0.010	<0.010	<0.011	<0.006	0.007	0.009
Ba	15.33	13.56	17.23	21.21	16.69	18.83	14.8	14.89	10.8	5.71	17.5	12.3
La	2.20	3.17	2.33	2.61	3.22	2.40	2.13	2.25	5.33	4.97	4.56	4.22
Ce	7.98	9.02	8.58	9.19	8.74	7.88	7.43	7.42	19.7	18.6	15.3	13.7
Pr	1.26	1.56	1.52	1.59	1.46	1.40	1.38	1.36	2.98	2.74	2.12	1.71
Nd	8.05	7.4	8.80	9.39	7.88	8.31	6.79	7.3	12.46	11.46	9.98	8.31
Sm	2.88	2.96	2.65	3.13	2.82	2.61	3.22	2.27	2.59	2.76	2.36	1.59
Eu	0.841	0.872	0.94	1.07	0.960	0.820	0.902	0.900	0.778	0.849	0.776	0.511
Gd	2.82	3.07	3.41	4.17	3.29	3.91	3.45	3.07	2.3	2.48	2.64	1.97
Tb	0.504	0.62	0.52	0.59	0.53	0.56	0.481	0.542	0.460	0.505	0.362	0.300
Dy	3.16	3.74	3.47	4.54	3.77	4.37	3.84	3.36	3.34	3.02	2.35	2.29
Ho	0.786	0.81	0.61	0.82	0.81	0.67	0.592	0.714	0.676	0.570	0.513	0.465
Er	1.73	1.95	1.79	1.98	2.13	2.06	2.10	1.76	1.81	1.25	1.33	0.908
Tm	0.269	0.217	0.24	0.32	0.23	0.36	0.221	0.252	0.304	0.204	0.247	0.136
Yb	1.69	1.86	1.87	1.57	1.75	1.79	1.96	1.96	1.68	1.66	1.86	1.30
Lu	0.232	0.234	0.25	0.23	0.20	0.20	0.196	0.205	0.282	0.341	0.207	0.166
Hf	0.931	0.950	0.700	0.826	0.640	0.670	0.518	0.934	0.602	0.928	0.736	0.761
Ta	0.081	0.087	0.043	0.131	0.084	0.067	0.127	0.068	0.225	0.141	0.121	0.129
Pb	3.7	3.82	2.14	2.93	2.97	2.87	2.35	2.79	1.58	1.65	1.85	1.85
Th	0.106	0.111	0.167	0.118	0.187	0.110	0.157	0.244	0.054	0.139	0.076	0.107
U	0.180	0.120	0.191	0.239	0.177	0.250	0.301	0.352	0.086	0.098	0.088	0.150
La_N/Sm_N	0.46	0.65	0.53	0.51	0.69	0.56	0.40	0.60	1.25	1.09	1.17	1.61

(continued)

concordia ages in the text are given as 2σ. The trace element composition of zircon was determined according to the method described above, but using ^{29}Si as the internal standard.

Quartz diorites

Fifty-eight zircon grains were selected. They are mostly euhedral and with prismatic habit (Fig. 9). Most crystals show well-developed oscillatory zoning typical of growth

Table 6: Continued

Rock type: Qtz diorite	Green amphibole							Tonalite					
Sample:	TT334	TT334	TT334	TT334	TT334	TT331	TT331	TT40	TT40	TT40	TT40	TT40	TT40
Li	7.61	6.74	8.02	9.83	8.56	4.96	5.83	7.23	6.33	5.04	3.25	8.4	7.48
B	3.75	2.85	3.2	<1.37	4.66	3.02	1.81	3.98	1.65	3.96	3.69	<1.74	2.52
Na	10760	11232	11526	10911	11479	14680	13250	17660	17048	15915	15713	17546	18901
Sc	42.4	42.1	44.3	43.8	42.3	60.4	58.9	84.0	106.31	86.1	95.51	98.2	79.8
Ti	2284	2160	2387	2201	2133	6311	6059	7483	8440	7738	7751	8028	8243
V	149	153	163	160	164	359	354	343	381	363	350	361	353
Cr	509	548	564	528	493	379	374	280	173	271	143	114	170
Co	58.4	62.4	63.1	57.9	60.0	63.5	62.5	44.6	47.3	45.1	47.2	45.2	50.2
Ni	250	247	260	257	256	300	290	55.4	57.5	61.6	93.0	59.3	118
Zn	96.7	88.9	99.5	94.3	75.8	78.6	83.7	167	152	166	147	176	146
Rb	1.454	0.963	2.5	4.72	1.106	1.028	1.336	3.82	3.91	3.48	14.65	3.73	3.47
Sr	18.6	18.3	19.8	18.2	16.3	32.0	26.6	30.7	32.8	25.9	28.6	28.5	33.6
Y	11.3	9.8	10.4	10.1	9.4	18.8	19.1	84.9	101.6	83.3	85.8	89.7	82.5
Zr	12.4	13.3	13.7	12.3	12.0	26.0	24.7	20.1	23.1	18.3	17.7	21.2	26.6
Nb	6.02	4.71	5.85	5.37	4.89	3.42	3.24	11.2	13.7	11.2	11.8	12.8	12.9
Cs	<0.007	<0.017	<0.015	0.02	<0.017	<0.010	<0.012	0.021	0.019	<0.01	0.136	0.657	0.019
Ba	7.10	6.69	8.01	5.39	7.86	12.4	12.5	39.5	31.9	37.7	30.2	35.9	34.7
La	6.27	5.91	6.56	5.89	5.37	5.66	5.43	4.76	6.04	4.67	5.14	5.55	5.58
Ce	21.0	19.5	20.9	18.9	20.2	18.1	19.2	32.7	42.5	34.8	37.5	37.9	43.1
Pr	2.80	2.46	2.73	2.43	2.64	2.75	2.64	8.04	10.04	7.97	8.79	8.88	8.98
Nd	10.45	9.64	10.01	10.21	11.69	11.52	12.85	46.58	60.13	49.4	50.63	50.58	50.48
Sm	1.85	1.93	1.58	1.96	1.72	3.27	3.16	17.01	21.16	15.34	15.52	16	16.31
Eu	0.70	0.69	0.63	0.62	0.51	0.979	0.902	3.39	3.12	3	3.13	3.07	3.05
Gd	2.07	1.83	1.39	1.62	1.99	3.84	3.86	16.99	19.6	14.02	16.27	17.08	16.07
Tb	0.280	0.260	0.246	0.260	0.267	0.599	0.519	2.51	3.22	2.28	2.68	2.94	2.48
Dy	2.38	1.81	2.19	1.38	1.65	3.93	3.81	16.42	20.29	15.41	17.74	16.96	15.76
Ho	0.421	0.391	0.415	0.347	0.407	0.827	0.805	3.23	3.75	3.17	3.35	3.53	3.47
Er	1.07	1.11	0.96	1.16	0.99	2.45	1.73	9.27	11.3	8.43	8.94	10.19	8.63
Tm	0.150	0.191	0.197	0.104	0.145	0.262	0.337	1.18	1.70	1.50	1.34	1.39	1.17
Yb	1.47	0.92	1.37	1.18	1.13	2.16	2.36	9.64	10.43	8.11	8.75	8.09	7
Lu	0.154	0.167	0.147	0.183	0.165	0.268	0.271	1.272	1.339	1.105	1.13	1.21	1.285
Hf	0.575	0.472	1.12	0.818	0.680	1.53	0.777	1.3	1.91	1.66	1.46	1.36	1.57
Ta	0.601	0.338	0.704	0.50	0.26	0.164	0.179	0.438	0.505	0.452	0.483	0.683	0.503
Pb	1.07	0.47	1.12	0.870	1.080	1.84	1.63	2.56	1.99	1.77	1.43	1.54	1.47
Th	0.130	0.105	0.106	0.120	0.060	0.272	0.198	0.014	0.030	<0.016	0.018	<0.019	<0.022
U	0.147	0.131	0.115	0.093	0.101	0.158	0.125	0.047	0.047	0.037	0.063	0.077	0.015
La_N/Sm_N	2.05	1.86	2.52	1.82	1.89	1.05	1.04	0.17	0.17	0.18	0.20	0.21	0.21

under magmatic conditions (e.g. Vavra *et al.*, 1996). A few zircons characterized by dark homogeneous cores and brighter rims with faint oscillatory zoning (e.g. crystal 34) were also found.

A total of 83 analyses were carried out and results are mostly concordant (Table 10); only few data reveal significant Pb loss. Ages obtained on domains with oscillatory zoning show a continuous spread from 527 ± 14 Ma to 473 ± 13 Ma (Fig. 10). The older ages were obtained in the inner portion of the grains, whereas the younger ones mostly pertain to the outer domains. One inner portion with low CL emission gave a

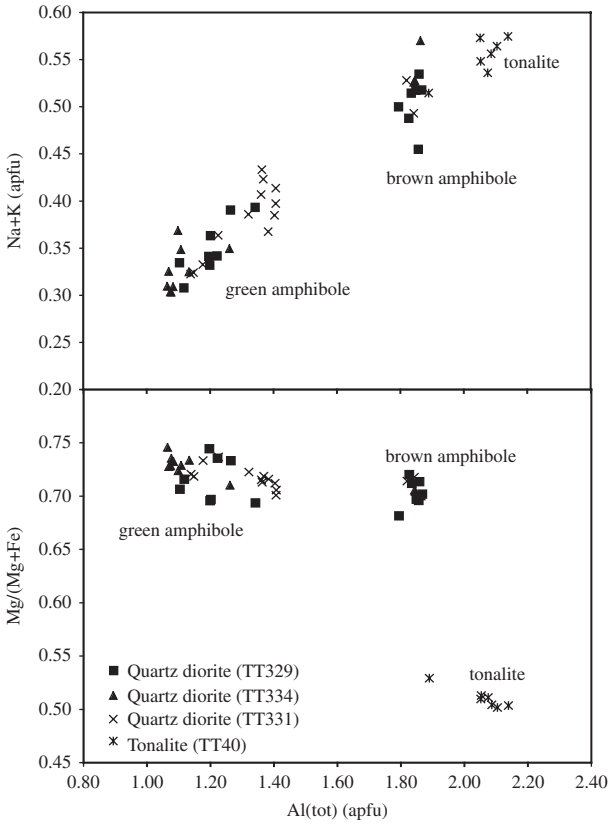

Fig. 6. Compositional variations in amphibole from quartz diorites and the tonalite.

concordant Pan-African age of 666 ± 19 Ma, which probably represents inheritance from the host basement. A few homogeneous zircons with low CL emission and faint oscillatory zoning yielded ages of 450 to 268 Ma, which do not represent magmatic events but resetting of the U–Pb system. Similar young ages observed by Bomparola *et al.* (2007) in the Lower Peak granites of NVL were attributed to fluid circulation and pervasive deformation. Intraplate reactivation processes, with fluid-assisted deformation leading to zircon resetting at about 450 Ma, have also been observed in NVL by Di Vincenzo *et al.* (2007).

Zircon trace element composition was determined on selected grains to constrain the origin of the age spread and better define the age of intrusion (Fig. 11 and Table 12). However, results show that, independently of the age, all grains have a similar chondrite-normalized REE patterns, with a steady decrease from HREE (about 2000 times Cl) to LREE and a positive Ce anomaly.

The core to rim continuity in crystal habit, the CL zoning patterns and the homogeneous chemical composition indicate a single-phase zircon growth. Because of the significant Pb loss and U–Pb system perturbation experienced by some of the selected zircon grains, the age of intrusion of quartz diorites is likely to approach the upper limit of the observed age spread. By considering all the analyses within error with the oldest age determination, a mean concordia age of 516 ± 3 Ma is obtained (21 analyses, MSWD = 0·0038; probability of concordance 0·95). This is retained as the best estimate for the intrusion age of the quartz diorites.

The younger apparent ages, mainly obtained from zircon rims, are probably related to minor and variable Pb loss, which may have caused the shift of data along the concordia. The uncertainty of the technique, unfortunately, means that it is not possible to appreciate if a U–Pb discordance occurs in these data. The late orogenic granitoid intrusions at 480 Ma that are widespread in NVL (e.g. Rocchi *et al.*, 1998) or even younger processes (see, e.g. Di Vincenzo *et al.*, 2007) may be responsible for the perturbation of the U–Pb zircon system. In particular, K–Ar ages on biotite from migmatitic gneisses of the nearby Husky Bluff yielded 484 ± 6 and 489 ± 6 Ma, interpreted as regional cooling ages, postdating the tectonic juxtaposition of the Wilson and Bowers terranes (Vita-Scaillet & Lombardo, 2003). External zircon domains recording a late opening of the U–Pb system at about 490 ± 3 Ma were also found in gabbronorites from the neighbouring mafic–ultramafic complex of the Niagara Icefall complex intruded at 514 ± 2 Ma (Tribuzio *et al.*, 2007).

Tonalite

Twenty-nine zircons were selected from the tonalite. They are structurally composite, with inherited cores surrounded by multiple overgrowths. Inner cores show rounded surfaces frequently cutting oscillatory and sector zoning (Fig. 9). A thin non-cathodoluminescent zone, generally attributed to segregated impurities, usually separates the domains. Up to three overgrowths were identified around the inner cores. In crystal 5, where the various overgrowths are well represented, a first domain around the inner core has rounded boundaries and low CL emission. The second overgrowth, with a thickness of up to 50 μm, has a prismatic habit and well-developed oscillatory zoning. The third overgrowth is about 10 μm thick and follows the prismatic habit of the adjacent domain, but with poorly developed oscillatory zoning. This thin outer overgrowth is common to many other zircon crystals.

Forty-seven age determinations were carried out on the various zircon domains from the tonalite, and 30 of them yielded concordant results (Table 11). Thirty-six analyses were carried out at a spot size of 20 μm and 11 at 10 μm spot size. This allowed us to analyse the outermost thin overgrowths, but at the expense of precision. The inner zircon domains yielded Neoproterozoic, Palaeoproterozoic and Archaean ages with concordia U–Pb ages clustering at 2600, 2300, 2250, 1080 and 890 Ma (Fig. 12). One inner domain gave an Early Cambrian age of 545 ± 18 Ma.

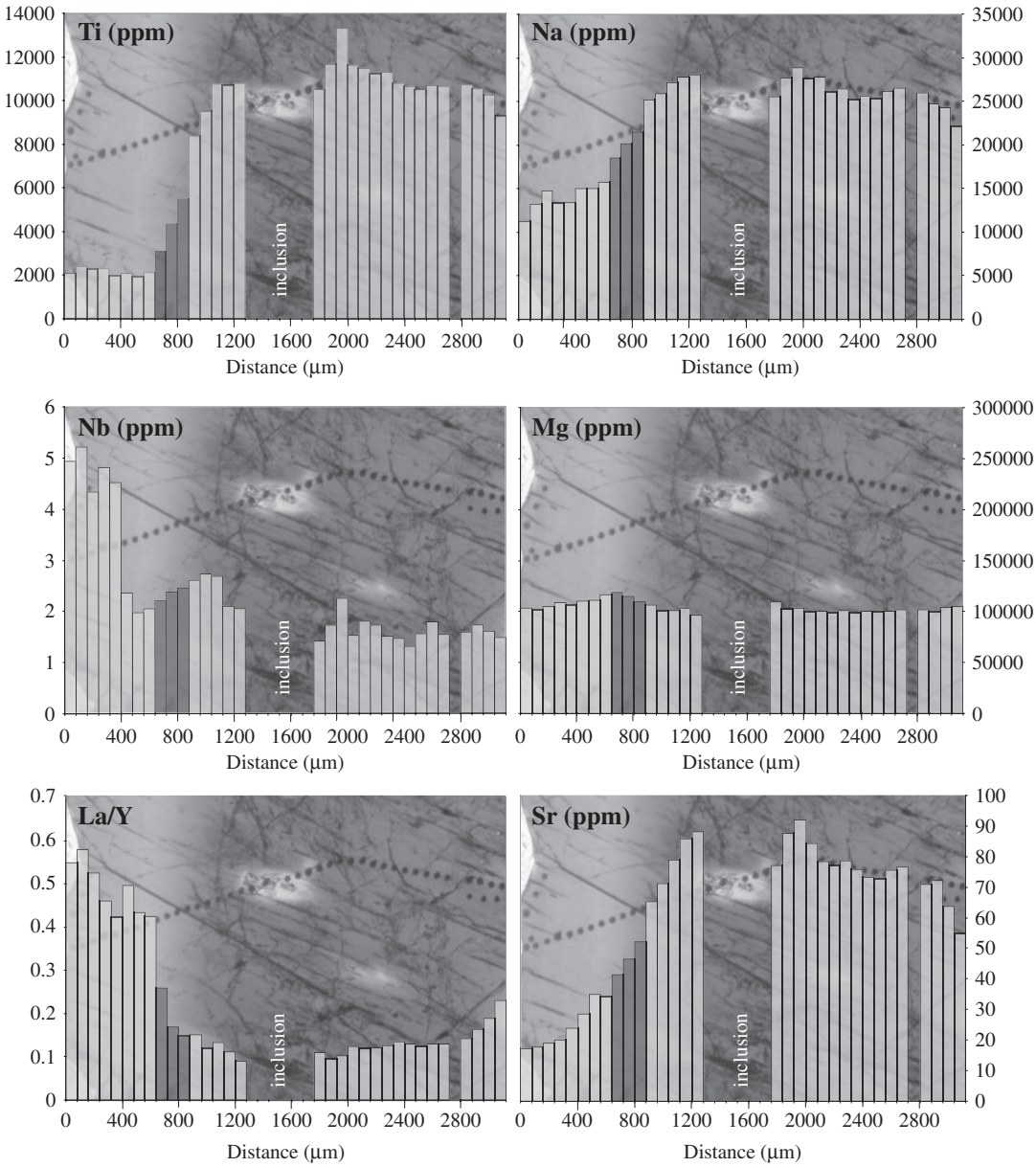

Fig. 7. Compositional profile by laser ablation (LA)-ICPMS across one amphibole grain in quartz diorite TT334. The dark grey bars mark the transition zone between green and brown amphibole. The break in the compositional profile is due to an inclusion.

The thin outermost rims (seven analyses) yielded younger ages, with a mean concordia age of 489 ± 8 Ma (2σ).

The trace element composition of zircons was determined on representative age domains in selected grains (Fig. 11 and Table 12). The REE pattern of the outermost rim at 489 Ma shows marked LREE depletion ($La = 0{\cdot}3$ times Cl chondrite) and HREE enrichment (1200 times Cl chondrite), with strong HREE fractionation ($Yb_N/Gd_N \gg 1$) and positive Ce anomaly. The REE pattern of the Early Cambrian domain parallels that of the thin external overgrowth at 489 Ma but with slightly higher HREE values. The domain at 890 Ma shows a REE pattern characterized by nearly flat HREE at about 100 times Cl chondrite and a marked negative Eu anomaly, suggesting equilibration with garnet (Rubatto, 2002) and plagioclase. Palaeoproterozoic domains have REE patterns similar to those of the younger domains but at higher concentrations (HREE at about 100 times Cl chondrite) and with marked negative Eu anomalies.

The definition of the age of emplacement of the tonalite body is not straightforward. The outermost thin zircon domains, showing oscillatory zoning and REE pattern typical of growth under magmatic conditions, probably crystallized from the tonalitic melt. However, their age

Table 7: Representative major element composition (wt %) of plagioclase

Rock type:	Qtz-Di	Qtz-Di	Qtz-Di	Qtz-Di	Qtz-Di	Qtz-Di	Qtz-Di	Qtz-Di	Qtz-Di	Qtz-Di	Qtz-Di	Qtz-Di	Tnl	Tnl	Tnl	Tnl	Tnl	Tnl
Sample:	TT329	TT329	TT329	TT334	TT334	TT334	TT334	TT334	TT331	TT331	TT331	TT331	TT40	TT40	TT40	TT40	TT40	TT40
SiO_2	59.96	60.11	60.37	57.71	57.74	57.75	57.86	57.48	59.74	59.84	59.60	59.43	58.02	58.40	57.91	58.18	58.29	56.98
TiO_2	0.06	0.00	0.00	0.00	0.00	0.03	0.00	0.00	0.00	0.00	0.03	0.05	0.01	0.02	0.00	0.00	0.00	0.03
Al_2O_3	25.21	24.84	24.85	26.51	26.66	26.62	27.04	27.07	25.49	25.56	25.45	25.49	26.47	26.37	26.83	26.77	26.54	27.00
Cr_2O_3	0.00	0.03	0.05	0.00	0.00	0.00	0.02	0.05	0.00	0.00	0.00	0.08	0.02	0.00	0.05	0.01	0.01	0.01
FeO_T	0.06	0.02	0.04	0.09	0.06	0.01	0.00	0.04	0.09	0.09	0.03	0.08	0.09	0.11	0.15	0.16	0.10	0.10
MnO	0.00	0.00	0.00	0.00	0.03	0.04	0.00	0.07	0.02	0.00	0.02	0.04	0.00	0.00	0.04	0.02	0.00	0.00
MgO	0.03	0.00	0.00	0.00	0.03	0.00	0.00	0.02	0.00	0.01	0.00	0.00	0.00	0.00	0.00	0.00	0.01	0.00
CaO	7.41	7.44	7.34	9.22	9.14	9.39	9.16	9.42	7.41	7.74	8.11	7.99	8.80	8.72	9.09	8.93	9.17	10.08
Na_2O	6.96	7.31	7.33	6.19	6.26	6.02	6.20	6.19	6.97	7.10	6.80	6.86	6.56	6.64	6.47	6.44	6.46	5.96
K_2O	0.10	0.13	0.07	0.23	0.17	0.21	0.12	0.13	0.21	0.21	0.15	0.18	0.14	0.15	0.12	0.15	0.15	0.10
Total	99.8	99.9	100.0	100.0	100.1	100.1	100.4	100.5	99.9	100.6	100.2	100.2	100.1	100.4	100.7	100.7	100.7	100.3
Si	2.67	2.68	2.69	2.59	2.59	2.59	2.58	2.57	2.66	2.66	2.65	2.65	2.60	2.60	2.58	2.59	2.59	2.55
Al	1.32	1.31	1.30	1.40	1.41	1.40	1.42	1.42	1.34	1.34	1.34	1.34	1.40	1.39	1.41	1.40	1.39	1.43
Ti	0.00	0.00	0.00	0.00	0.00	0.00	0.00	0.00	0.00	0.00	0.00	0.00	0.00	0.00	0.00	0.00	0.00	0.00
Cr	0.00	0.00	0.00	0.00	0.00	0.00	0.00	0.00	0.00	0.00	0.00	0.00	0.00	0.00	0.00	0.00	0.00	0.00
Mg	0.00	0.00	0.00	0.00	0.00	0.00	0.00	0.00	0.00	0.00	0.00	0.00	0.00	0.00	0.00	0.00	0.00	0.00
Fe^{2+}	0.00	0.00	0.00	0.00	0.00	0.00	0.00	0.00	0.00	0.00	0.00	0.00	0.00	0.00	0.01	0.01	0.00	0.00
Mn	0.00	0.00	0.00	0.00	0.00	0.00	0.00	0.00	0.00	0.00	0.00	0.00	0.00	0.00	0.00	0.00	0.00	0.00
Ca	0.35	0.36	0.35	0.44	0.44	0.45	0.44	0.45	0.35	0.37	0.39	0.38	0.42	0.42	0.43	0.43	0.44	0.48
Na	0.60	0.63	0.63	0.54	0.54	0.52	0.54	0.54	0.60	0.61	0.59	0.59	0.57	0.57	0.56	0.56	0.56	0.52
K	0.01	0.01	0.00	0.01	0.01	0.01	0.01	0.01	0.01	0.01	0.01	0.01	0.01	0.01	0.01	0.01	0.01	0.01
An mol %	36.8	35.7	35.5	44.6	44.2	45.7	44.6	45.4	36.6	37.1	39.4	38.8	42.2	41.7	43.4	43.0	43.6	48.0

Qtz-Di, quartz diorite; Tnl, tonalite.

of 489 ± 8 Ma may not represent the age of the tonalite intrusion. Similarly to quartz diorites, younger tectonic reactivation processes may have caused the resetting of the U–Pb system in zircon. Although current data do not allow us to define the emplacement age of the tonalite body, the large crustal contribution from the host basement (see next section) in the petrogenesis of the tonalitic melt is noteworthy for the present study.

The host basement (biotite gneiss)

Twenty-seven zircons were selected from the Bt-gneiss. They are prismatic, and under CL they show inherited cores and multiple overgrowths similar to those observed in the tonalite sample. Inner cores frequently display relics of oscillatory zoning (Fig. 9) that are truncated by rounded boundaries, suggesting resorption. The outermost overgrowths have low luminescence.

A total of 33 analyses were carried out on this sample, and only 15 analyses gave concordant ages (Table 11, Fig. 13). Discordant ages are scattered and do not yield additional geochronological information. The densest age clusters are at about 600 and 750 Ma. These age peaks agree with two of the major Pan-African events responsible for the accretion of Gondwana (e.g. Meert, 2003). There is a minor peak at about 1050 Ma, and four concordia ages from inner cores are between 2600 and 2300 Ma. One low luminescence overgrowth in zircon 3 yields a Cambrian age at 536 ± 18 Ma. Most of the age clusters of the Bt-gneiss resemble those of the tonalite. Zircons from the Bt-gneiss show chondrite-normalized REE patterns typical of growth under magmatic conditions, with marked negative Eu anomaly (Fig. 11 and Table 12). No evidence of equilibration with garnet was observed.

EVIDENCE FOR OPEN-SYSTEM EVOLUTION OF QUARTZ DIORITES

The texture and mineral chemistry of quartz diorites suggest the presence of two distinct mineral assemblages not in chemical equilibrium: (1) clinopyroxene included in brown amphibole (hereafter clinopyroxene-I) + brown amphibole + dark mica; (2) clinopyroxene in the matrix (hereafter clinopyroxene-II) + green

Table 8: Representative trace element composition of plagioclase and titanite (ppm)

Rock type:	Qtz-Di	Qtz-Di	Qtz-Di	Tnl	Qtz-Di	Qtz-Di	Qtz-Di	Qtz-Di	Qtz-Di
Sample:	TT334	TT329	TT331	TT40	TT329	TT329	TT329	TT329	TT329
Mineral:	Pl	Pl	Pl	Pl	Tit	Tit	Tit	Tit	Tit
Li	0.350	0.240	0.169	0.190	<0.28	<0.292	0.590	<0.288	<0.28
B	7.89	9.46	4.50	3.81	<2.59	<1.94	<2.12	<1.66	<2.59
Sc	1.47	4.06	1.77	0.547	1.99	2.98	3.56	1.67	1.99
Ti	11.4	21.3	19.5	24.8	–	–	–	–	–
V	<0.16	0.465	0.222	1.64	284	297	707	290	284
Cr	4.26	<1.70	2.58	3.03	–	–	–	–	–
Co	0.114	0.034	0.152	0.186	–	–	–	–	–
Ni	1.18	0.480	0.613	1.68	–	–	–	–	–
Zn	4.91	1.07	2.10	2.43	–	–	–	–	–
Rb	3.07	0.138	0.128	0.145	<0.083	0.107	<0.068	0.102	<0.083
Sr	744	722	665	641	50.5	33.7	40.7	52.4	50.5
Y	0.030	0.022	0.024	0.125	750	852	1036	637	750
Zr	<0.038	0.034	<0.025	0.168	714	497	599	440	714
Nb	<0.014	<0.013	<0.011	0.024	694	568	646	873	694
Cs	0.030	0.114	0.014	0.028	–	–	–	–	–
Ba	131	127	118	61.0	<0.196	<0.148	<0.20	0.25	<0.196
La	3.02	1.98	1.45	2.41	995	681	1712	706	995
Ce	2.91	2.40	1.44	4.52	2853	2091	4281	1938	2853
Pr	0.151	0.143	0.066	0.426	387	309	516	278	387
Nd	0.427	0.354	0.130	0.957	1564	1276	1813	1097	1564
Sm	0.073	<0.047	<0.047	0.136	268	250	301	203	268
Eu	0.259	0.336	0.248	0.589	51.8	49.9	95.0	55.6	51.8
Gd	<0.051	0.073	<0.079	0.182	199	199	231	179	199
Tb	<0.001	<0.006	0.009	0.027	26.3	26.8	29.1	21.4	26.3
Dy	0.046	<0.019	0.043	0.065	157	173	184	131	157
Ho	<0.010	0.007	<0.009	<0.016	28.3	32.1	33.3	22.8	28.3
Er	<0.044	<0.036	<0.040	<0.057	76.0	87.5	95.5	65.7	76.0
Tm	<0.007	<0.007	<0.009	<0.017	11.5	11.5	15.3	10.1	11.5
Yb	<0.046	<0.043	<0.091	<0.079	83.6	88.6	111.3	58.5	83.6
Lu	<0.011	<0.007	<0.009	<0.013	11.0	11.4	15.2	9.4	11.0
Hf	<0.051	<0.032	<0.045	<0.077	33.9	27.4	29.6	22.4	33.9
Ta	<0.017	<0.012	<0.008	0.017	28.5	23.8	31.3	36.7	28.5
Pb	25.08	44.63	24.61	12.55	20.6	10.2	34.9	12.6	20.6
Th	0.016	<0.007	<0.008	0.018	449	195	788	283	449
U	0.009	<0.006	0.009	0.548	64.2	34.1	225.5	44.4	64.2

Qtz-Di, quartz diorite; Tnl, tonalite; Pl, plagioclase; Tit, titanite.

amphibole + plagioclase + quartz + accessory phases. In particular, the minerals from the second assemblage show marked LREE enrichment over HREE and Ti depletion.

The two mineral assemblages may be interpreted as the product of crystallization of a single melt through simple closed-system fractional crystallization. This hypothesis, however, contrasts with both rock texture (Fig. 3) and mineral trace element composition, and in particular with the chemical profile across amphibole (Fig. 7). The transition from brown to green amphibole, occurring in about 200 μm, is sharp and sudden. The narrow interface precludes the continuous growth of amphibole from a melt undergoing differentiation through fractional crystallization in a closed system or through another processes implying a steady change of melt composition, such as assimilation and fractional crystallization (AFC). In either case, zoning would be more gradual. The matrix assemblage may alternatively be interpreted as the product of crystallization of a trapped melt. This process may lead to extreme trace element enrichments in the crystallizing

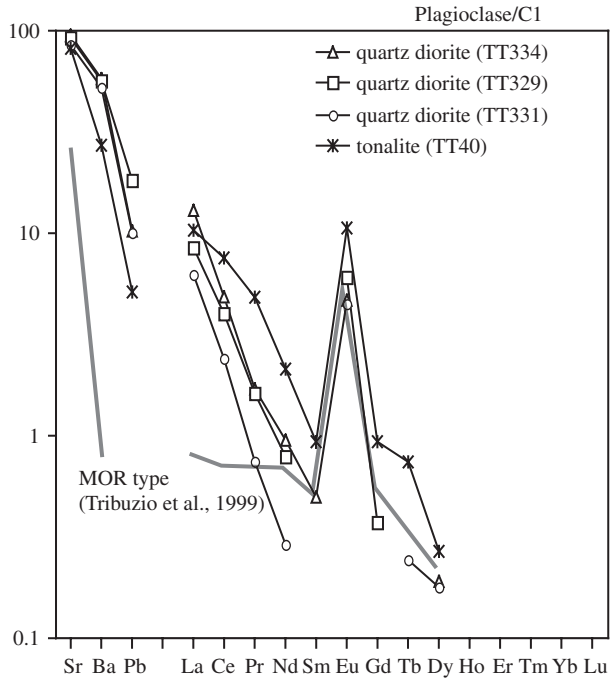

Fig. 8. Chondrite-normalized incompatible element patterns for plagioclase from quartz diorites and tonalite. The mean composition of plagioclase from a MOR gabbroic rock (Tribuzio *et al.*, 1999) is shown for comparison. Normalization values are from Anders & Ebihara (1982).

products (Cawthorn, 1996). However, crystallization of a trapped melt is also unlikely, as this contrasts with the high modal proportion of matrix minerals (20–70 vol. %) in the studied samples. The above considerations lead us to suppose that the two mineral assemblages were derived from two distinct melt pulses. Quartz diorites thus formed in an open system in which a crystal mush consisting of brown amphibole (± clinopyroxene ± biotite) interacted with a compositionally different melt.

PARENTAL MELTS OF QUARTZ DIORITES

Because of the composite and cumulus nature of the quartz diorites, the bulk rock would give an average composition of the two mineral assemblages and prevent accurate definition of the chemical composition of the parental melts. We therefore adopted a different approach; that is, equilibrium melts with the two distinct mineral assemblages were computed from mineral compositions by applying solid/liquid partition coefficients. Melts in equilibrium with clinopyroxene and amphibole from the two mineral assemblages were calculated with the solid/liquid partition coefficients reported in Electronic Appendix 3. Crystal chemical differences between the two clinopyroxene and amphibole generations are almost negligible and do not justify the adoption of different sets of solid/liquid partition coefficients. The presence of quartz in the second mineral assemblage, however, suggests that the parental melt was more SiO_2-rich than that in equilibrium with clinopyroxene-I and brown amphibole. Slightly higher $D^{solid/liquid}$ values are therefore expected for elements with high charge/ionic radius ($\mathcal{Z}/r$) ratios (e.g. Tiepolo *et al.*, 2007). None the less, because of the uncertainty in SiO_2 differences and the lack of a large self-consistent set of $D^{S/L}$ values at higher SiO_2 contents, we adopted the same set of values for both systems. The trace element composition of the melt in equilibrium with the second mineral assemblage may thus be slightly overestimated for element with high $\mathcal{Z}/r$ ratios such as REE and HFSE; however, no inter-element fractionation is expected.

Table 9: Representative major element composition (wt %) of amphibole in tonalite

Sample:	TT40	TT40	TT40	TT40	TT40	TT40	TT40
SiO_2	42.99	42.40	42.74	44.25	42.88	43.05	42.61
TiO_2	1.19	1.17	1.26	1.14	1.27	1.20	1.22
Al_2O_3	11.53	11.96	11.79	10.75	11.70	11.55	11.79
Cr_2O_3	0.01	0.07	0.00	0.04	0.06	0.04	0.00
FeO_T	17.35	17.38	17.86	17.12	17.38	17.16	17.47
MnO	0.38	0.29	0.37	0.39	0.28	0.33	0.40
MgO	10.24	9.87	10.18	10.79	10.19	10.00	9.86
CaO	11.31	11.52	11.79	11.59	11.79	11.83	11.59
Na_2O	1.30	1.33	1.29	1.27	1.24	1.34	1.24
K_2O	0.87	0.95	0.94	0.78	0.91	0.93	1.03
Total	97.16	96.93	98.22	98.12	97.70	97.43	97.20
Si	6.50	6.44	6.42	6.60	6.46	6.49	6.46
Ti	0.14	0.13	0.14	0.13	0.14	0.14	0.14
Al	2.05	2.14	2.09	1.89	2.08	2.05	2.11
Cr	0.00	0.01	0.00	0.00	0.01	0.00	0.00
Fe	2.19	2.21	2.24	2.14	2.19	2.17	2.21
Mn	0.05	0.04	0.05	0.05	0.04	0.04	0.05
Mg	2.30	2.23	2.28	2.40	2.28	2.25	2.22
Ca	1.83	1.87	1.90	1.85	1.90	1.91	1.88
Na	0.38	0.39	0.38	0.37	0.36	0.39	0.37
K	0.17	0.18	0.18	0.15	0.17	0.18	0.20
Mg/(Mg + Fe)	0.51	0.50	0.50	0.53	0.51	0.51	0.50
Na + K	0.55	0.57	0.56	0.51	0.54	0.57	0.56

Cations are normalized to 23 oxygens.

Melt-I: clinopyroxene-I and brown amphibole

The melt composition calculated from the average composition of clinopyroxene-I (Fig. 14; Table 13) is characterized

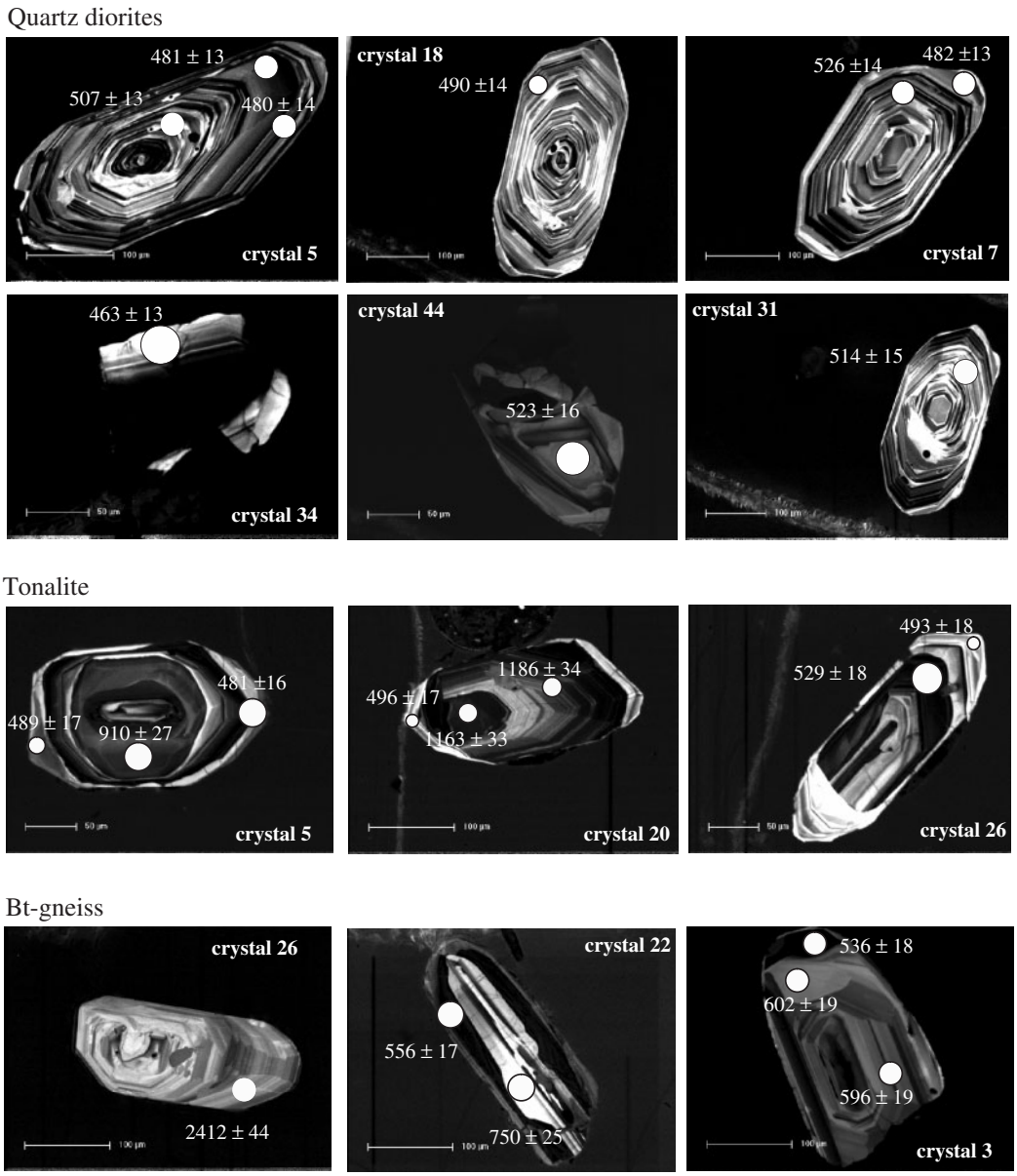

Fig. 9. Cathodoluminescence images of representative zircons from quartz diorites, tonalite and Bt-gneiss. The location of the spot analysis and U–Pb concordia ages with 2σ errors are also shown.

by LREE enrichment over HREE ($La_N = 2{\cdot}7$; $La_N/Yb_N = 12{\cdot}8$), which are nearly flat ($Dy_N/Yb_N = 1{\cdot}0$) at about 0·2 times N-MORB. A slight positive Sr anomaly is observed, whereas Th, U and Pb are strongly enriched (>100 times) relative to N-MORB. Li is about 20 times N-MORB.

The average composition of the melt in equilibrium with brown amphibole (Table 13) shows an incompatible trace element pattern characterized by a LREE enrichment over HREE comparable with that observed in the melt from clinopyroxene-I ($La_N/Yb_N = 11$) but with slightly higher contents; for instance, HREE are nearly flat at about 0·5 times N-MORB (Fig. 14). A weak negative Sr anomaly is observed; Nb and Ta are about two times N-MORB and thus depleted relative to both LREE and LILE. The Nb_N/Ta_N ratio approaches unity. Zr and Hf contents are similar to HREE concentrations (about 0·4 times N-MORB). U is more than 100 times N-MORB. Th, Pb and Rb (about 20–30 times N-MORB) are enriched relative to LREE, whereas Ba is less than 10 times N-MORB. Li and B are about 10 and 600 times N-MORB.

Most of trace elements show a similar fractionation in the liquid computed from clinopyroxene-I and brown

Table 10: U–Pb isotope ratios and apparent ages for quartz diorites

Sample	Run	Spot (μm)	Grain-position	$^{206}Pb/^{238}U$	1σ	$^{207}Pb/^{235}U$	1σ	Apparent ages (Ma)					
								$^{206}Pb/^{238}U$	1σ	$^{207}Pb/^{235}U$	1σ	Concordia age	2σ
TT327	Oc23a05	25	Z1-C	0.0836	0.0009	0.6201	0.0113	518	6	490	9	—	—
TT327	Oc23a06	25	Z1-C	0.0814	0.0009	0.6124	0.0111	505	6	485	9	—	—
TT327	Oc23a07	25	Z4-R	0.0811	0.0009	0.6110	0.0114	503	6	484	9	—	—
TT327	Oc23a08	25	Z4-C	0.0821	0.0010	0.6196	0.0123	509	6	490	10	—	—
TT327	Oc23a09	25	Z3-R	0.0770	0.0010	0.6020	0.0128	478	6	479	10	478	12
TT327	Oc23a10	25	Z3-C	0.0803	0.0011	0.6298	0.0149	498	7	496	12	498	12
TT327	Oc23a11	25	Z8-C	0.0831	0.0010	0.7112	0.0139	515	6	546	11	—	—
TT327	Oc23a12	25	Z8-C	0.0791	0.0011	0.6139	0.0154	491	7	486	12	490	13
TT327	Oc23a13	25	Z11-C	0.0778	0.0010	0.6058	0.0129	483	6	481	10	483	12
TT327	Oc23a14	25	Z11-C	0.0818	0.0009	0.6102	0.0120	507	6	484	9	—	—
TT327	Oc23a15	25	Z12-C	0.0796	0.0009	0.6121	0.0116	494	6	485	9	492	11
TT327	Oc23a16	25	Z12-C	0.0819	0.0011	0.5750	0.0118	507	7	461	9	—	—
TT327	Oc23a17	25	ZA-C	0.0819	0.0010	0.6144	0.0117	507	6	486	9	—	—
TT327	Oc23a18	25	Z16-C	0.0793	0.0010	0.6287	0.0134	492	6	495	11	492	11
TT327	Oc23a19	25	Z16-C	0.0837	0.0010	0.6591	0.0136	518	6	514	11	517	12
TT327	Oc23a23	25	Z17-C	0.0855	0.0012	0.6628	0.0179	529	7	516	14	527	14
TT327	Oc23a24	25	Z17-I	0.0826	0.0011	0.6540	0.0161	512	7	511	13	512	13
TT327	Oc23a25	25	Z20-C	0.0821	0.0010	0.6470	0.0133	509	6	507	10	508	11
TT327	Oc23a26	25	Z21-C	0.0798	0.0010	0.6257	0.0138	495	6	493	11	495	12
TT327	Oc23a27	25	Z21-R	0.0819	0.0010	0.6226	0.0126	508	6	492	10	—	—
TT327	Oc23a28	25	Z30-C	0.0827	0.0011	0.6503	0.0141	512	7	509	11	512	13
TT327	Oc23a29	25	Z30-C	0.0831	0.0011	0.6576	0.0143	515	7	513	11	514	13
TT331	Oc23a30	25	Z1-R	0.0801	0.0009	0.6279	0.0123	497	6	495	10	496	11
TT331	Oc23a31	25	Z1-C	0.0835	0.0012	0.6534	0.0188	517	8	511	15	516	14
TT331	Oc23a32	25	Z1-R	0.0787	0.0011	0.6132	0.0140	489	7	486	11	488	13
TT331	Oc23a33	25	Z4-C	0.0842	0.0011	0.6692	0.0154	521	7	520	12	521	12
TT331	Oc23a34	25	Z4-C	0.0807	0.0010	0.6469	0.0137	501	6	507	11	501	12
TT331	Oc23a35	25	Z4-R	0.0766	0.0010	0.6039	0.0139	476	6	480	11	476	12
TT331	Oc23a36	25	Z4-R	0.0767	0.0009	0.6023	0.0123	477	6	479	10	477	11
TT331	Oc23a37	25	Z4-R	0.0798	0.0012	0.6341	0.0183	495	7	499	14	495	14
TT328	No28a05	25	Z1-R	0.0761	0.0011	0.5930	0.0204	473	7	473	16	473	13
TT328	No28a06	25	Z3-R	0.0779	0.0011	0.6110	0.0211	484	7	484	17	484	13
TT328	No28a07	25	Z5-R	0.0774	0.0011	0.6035	0.0208	481	7	479	16	481	13
TT328	No28a08	25	Z7-R	0.0775	0.0011	0.6447	0.0221	481	7	505	17	482	13
TT328	No28a09	25	Z7-C	0.0848	0.0012	0.6786	0.0235	524	8	526	18	526	14
TT328	No28a10	25	Z8-C	0.0839	0.0012	0.6786	0.0237	519	7	526	18	520	14
TT328	No28a11	25	Z8-C	0.0799	0.0012	0.6372	0.0230	496	8	501	18	496	15
TT328	No28a12	25	Z10-C	0.0843	0.0013	1.4260	0.0497	522	8	900	31	—	—
TT328	No28a13	25	Z11-R	0.0778	0.0012	0.6091	0.0234	483	8	483	19	483	15
TT328	No28a14	25	Z11-C	0.0787	0.0012	0.6172	0.0220	488	8	488	17	488	14
TT328	No28a15	25	Z12-C	0.0822	0.0012	0.6465	0.0230	509	8	506	18	509	15
TT328	No28a16	25	Z13-C	0.0797	0.0012	0.6277	0.0224	494	7	495	18	494	14
TT328	No28a17	25	Z15-C	0.0812	0.0012	0.6424	0.0234	503	8	504	18	503	15
TT328	No28a18	25	Z17-R	0.0779	0.0012	0.6191	0.0221	484	7	489	17	484	14
TT328	No28a19	25	Z17-C	0.0780	0.0012	0.6089	0.0212	484	7	483	17	484	14

(continued)

Table 10: Continued

Sample	Run	Spot (μm)	Grain-position	$^{206}Pb/^{238}U$	1σ	$^{207}Pb/^{235}U$	1σ	Apparent ages (Ma)					
								$^{206}Pb/^{238}U$	1σ	$^{207}Pb/^{235}U$	1σ	Concordia age	2σ
TT328	No28a20	25	Z18-R	0.0789	0.0012	0.6279	0.0217	489	7	495	17	490	14
TT328	No28a21	25	Z20-C	0.0578	0.0009	0.4759	0.0165	362	6	395	14	—	—
TT328	No28a22	25	Z20-R	0.0789	0.0012	0.6216	0.0221	490	7	491	17	490	14
TT328	No28a23	25	Z20-R	0.0773	0.0012	0.6024	0.0220	480	7	479	17	480	14
TT328	No28a24	25	Z23-C	0.0775	0.0012	0.5972	0.0219	481	7	475	17	481	14
TT328	No28a25	25	Z23-R	0.0783	0.0011	0.6206	0.0223	486	7	490	18	486	14
TT328	No28a26	25	Z24-C	0.0830	0.0012	0.6553	0.0230	514	8	512	18	514	15
TT328	No28a27	25	Z26-R	0.0778	0.0012	0.6077	0.0214	483	7	482	17	483	14
TT328	No28a28	25	Z27-R	0.0774	0.0012	0.6103	0.0211	481	7	484	17	481	14
TT328	No28a29	25	Z28-R	0.0786	0.0012	0.6108	0.0223	488	8	484	18	487	15
TT328	No28a30	25	Z29-R	0.0774	0.0012	0.6020	0.0210	480	7	479	17	480	14
TT328	No28a34	25	Z31-C	0.0832	0.0012	0.6582	0.0230	515	8	514	18	514	15
TT328	No28a35	25	Z33-C	0.0843	0.0013	0.6706	0.0230	522	8	521	18	522	15
TT328	No28a36	25	Z39-C	0.0772	0.0012	0.6751	0.0247	480	8	524	19	—	—
TT328	No28a37	25	Z37-C	0.0625	0.0010	0.4759	0.0164	391	6	395	14	391	12
TT328	No28a38	25	Z40-R	0.0792	0.0012	0.6137	0.0224	492	8	486	18	491	14
TT328	No28a39	25	Z41-R	0.0773	0.0012	0.6052	0.0216	480	7	481	17	480	14
TT328	No28a40	25	Z41-C	0.0798	0.0012	0.6257	0.0225	495	7	493	18	495	14
TT328	No28a41	25	Z45-C	0.1088	0.0016	0.9498	0.0340	666	10	678	24	666	19
TT328	No28a42	25	Z46-C	0.0400	0.0006	0.4777	0.0164	253	4	397	14	—	—
TT328	No28a43	25	Z48-C	0.0592	0.0009	0.4531	0.0155	371	5	379	13	371	11
TT328	No28a44	25	Z44-C	0.0844	0.0013	0.6749	0.0271	523	8	524	21	523	16
TT328	No28a45	25	Z42-R	0.0764	0.0011	0.6151	0.0210	475	7	487	17	475	13
TT328	No28a46	25	Z43-C	0.0729	0.0011	0.5667	0.0194	453	7	456	16	454	13
TT328	No28a47	25	Z34-R	0.0747	0.0011	0.5731	0.0202	464	7	460	16	463	13
TT328	No28a48	25	Z32-C	0.0707	0.0011	0.5370	0.0186	440	7	436	15	440	13
TT328	No28a49	25	Z22-C	0.0424	0.0007	0.3137	0.0111	268	4	277	10	268	8.3
TT328	No28a50	25	Z9-C	0.0884	0.0014	0.6546	0.0228	546	8	511	18	—	—
TT328	No28a51	25	Z10-C	0.0796	0.0013	0.6362	0.0250	494	8	500	20	495	15
TT328	No28a52	25	Z6-C	0.0738	0.0011	0.5762	0.0202	459	7	462	16	460	14
TT328	No28a53	25	Z5-R	0.0773	0.0012	0.5953	0.0219	480	8	474	17	480	14
TT328	Oc31a04	25	Z3-C	0.0777	0.0009	0.5999	0.0064	482	6	477	5	476	8
TT328	Oc31a05	25	Z26-C	0.0849	0.0011	0.6792	0.0096	525	6	526	7	526	12
TT328	Oc31a06	25	Z26-I	0.0825	0.0012	0.6740	0.0189	511	7	523	15	512	14
TT328	Oc31a07	25	Z27-C	0.0824	0.0012	0.6631	0.0175	510	7	517	14	511	14
TT328	Oc31a08	25	Z28-C	0.0807	0.0010	0.6315	0.0083	500	6	497	7	496	10
TT328	Oc31a09	25	Z29-C	0.0849	0.0011	0.6701	0.0126	526	7	521	10	524	12
TT328	Oc31a10	25	Z5-C	0.0817	0.0011	0.6619	0.0155	506	7	516	12	507	13

Grain-position: C, core; I, intermediate; R, rim. —, discordant age.

amphibole, but a difference of about two times in the absolute values is observed. These differences are probably related to uncertainties in the consistency of the $D^{S/L}$ between amphibole and clinopyroxene. Therefore, in the discussion below, the average composition between the melt computed from clinopyroxene-I and from brown amphibole (hereafter Melt-I) will be considered. This approach allows us to overcome the uncertainties related to the choice of $D^{S/L}$ and to obtain information on the concentration of elements (such as Ba,

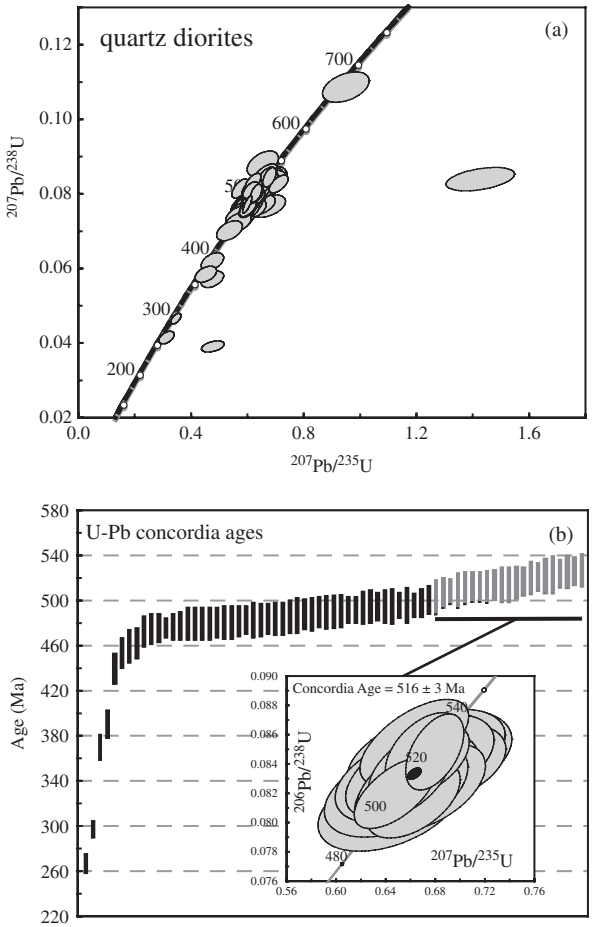

Fig. 10. Geochronological results for quartz diorites. (a) $^{238}U/^{206}Pb$ vs $^{235}U/^{207}Pb$ concordia diagram. (b) U–Pb concordia age distribution; grey boxes are the data used to calculate the mean concordia age reported in the inset (see text for details). Box heights and ellipses are 2σ errors.

Rb and Ta) that are below detection limits in clinopyroxene.

Melt-II: clinopyroxene-II and green amphibole

The mean incompatible element pattern of melt in equilibrium with clinopyroxene-II (Fig. 14; Table 13) is characterized by a strong enrichment of LREE over HREE, which are convex-downward ($Dy_N/Yb_N = 0{\cdot}79$) at about 0·2 times N-MORB. LREE contents are around 10 times N-MORB and the La_N/Yb_N ratio is approximately three times higher than in melt-I (around 38). No negative Sr and Eu anomalies are observed. The low Ti contents (less than 0·1 times N-MORB) produce a marked negative anomaly in the incompatible trace element pattern. Nb is depleted relative to LREE and shows normalized values similar to those of melt-I. Li, B, Th, Pb and U are enriched relative to all other elements.

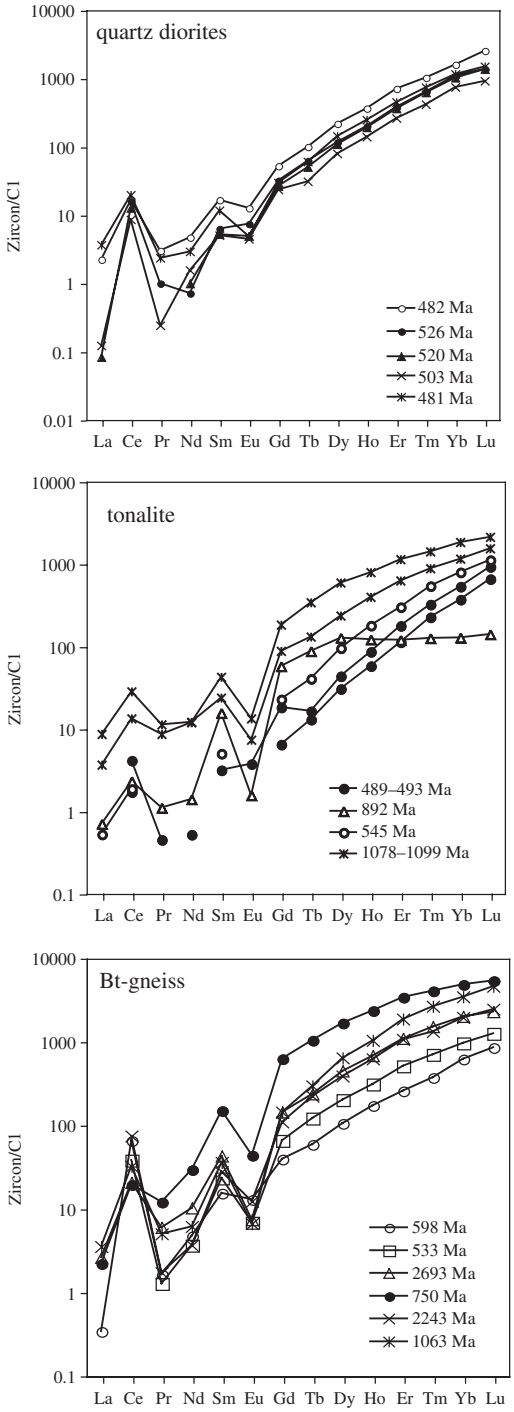

Fig. 11. Chondrite-normalized rare earth element pattern for zircons from quartz diorites, tonalite and Bt-gneiss. Normalization values are from Anders & Ebihara (1982).

The melt in equilibrium with green amphibole (Fig. 14; Table 13) has a N-MORB normalized incompatible element pattern that parallels that of many elements that are computed from clinopyroxene-II. HREE contents are slightly higher but with the same convex-down pattern.

Table 11: U–Pb isotope ratios and apparent ages for tonalite and Bt-gneiss

Sample	Run	Rock type	Spot (μm)	Grain-position	$^{206}Pb/^{238}U$	1σ	$^{207}Pb/^{235}U$	1σ	Apparent ages (Ma)					
									$^{206}Pb/^{238}U$	1σ	$^{207}Pb/^{235}U$	1σ	Concordia age	2σ
TT40	No30a05	Tnl	25	Z1-R	0·0750	0·0013	0·5808	0·0182	466	8	465	15	465	16
TT40	No30a06	Tnl	25	Z1-I	0·4227	0·0070	8·1054	0·2135	2273	38	2243	59	2243	47
TT40	No30a07	Tnl	25	Z1-C	0·4279	0·0071	8·3207	0·2200	2296	38	2267	60	2270	47
TT40	No30a08	Tnl	25	Z3-C	0·0970	0·0016	1·9847	0·0521	597	10	1110	29	—	—
TT40	No30a09	Tnl	25	Z4-C	0·4322	0·0072	8·7139	0·2289	2315	39	2309	61	2309	47
TT40	No30a10	Tnl	25	Z4-R	0·3503	0·0060	6·8208	0·1808	1936	33	2088	55	—	—
TT40	No30a11	Tnl	25	Z5-R	0·0773	0·0013	0·6135	0·0164	480	8	486	13	481	16
TT40	No30a12	Tnl	25	Z5-C	0·1505	0·0026	1·4799	0·0395	904	15	922	25	910	27
TT40	No30a13	Tnl	25	Z6-C	0·1846	0·0032	1·9069	0·0542	1092	19	1084	31	1089	32
TT40	No30a14	Tnl	25	Z7-C	0·0784	0·0013	0·9244	0·0245	487	8	665	18	—	—
TT40	No30a15	Tnl	25	Z9-C	0·0937	0·0016	0·7415	0·0197	577	10	563	15	574	18
TT40	No30a16	Tnl	25	Z10-C	0·3234	0·0053	5·0009	0·1329	1806	30	1820	48	1815	43
TT40	No30a17	Tnl	25	Z10-R	0·0838	0·0015	0·8012	0·0222	519	9	598	17	—	—
TT40	No30a18	Tnl	25	Z11-C	0·0935	0·0016	0·7371	0·0199	576	10	561	15	572	19
TT40	No30a19	Tnl	25	Z12-C	0·1215	0·0021	1·2488	0·0334	739	13	823	22	—	—
TT40	No30a20	Tnl	25	Z13-C	0·0376	0·0007	0·2777	0·0074	238	4	249	7	—	—
TT40	No30a21	Tnl	25	Z14-R	0·1821	0·0033	1·8690	0·0568	1079	19	1070	33	1076	33
TT40	No30a22	Tnl	25	Z14-C	0·1743	0·0032	1·7666	0·0560	1036	19	1033	33	1035	33
TT40	No30a26	Tnl	25	Z18-C	0·4149	0·0071	8·0948	0·2185	2237	38	2242	61	2241	48
TT40	No30a27	Tnl	25	Z19-C	0·1602	0·0027	1·6431	0·0462	958	16	987	28	966	29
TT40	No30a28	Tnl	25	Z20-C	0·1973	0·0033	2·1494	0·0569	1161	20	1165	31	1163	33
TT40	No30a29	Tnl	25	Z20-R	0·2011	0·0034	2·2351	0·0595	1181	20	1192	32	1186	34
TT40	No30a30	Tnl	25	Z22-C	0·5046	0·0085	15·4756	0·4124	2634	44	2845	76	—	—
TT40	No30a31	Tnl	25	Z26-R	0·0752	0·0013	0·6442	0·0181	468	8	505	14	—	—
TT40	No30a32	Tnl	25	Z26-C	0·0884	0·0015	0·7048	0·0189	546	9	542	14	545	18
TT40	No30a33	Tnl	25	Z28-R	0·5089	0·0090	12·5717	0·3391	2652	47	2648	71	2648	51
TT40	No30a34	Tnl	25	Z29-C	0·1899	0·0034	2·0359	0·0565	1121	20	1128	31	1124	34
TT40	No30a35	Tnl	25	Z33-C	0·1086	0·0018	1·1175	0·0297	665	11	762	20	—	—
TT40	No30a36	Tnl	25	Z34-C	0·0747	0·0013	0·5913	0·0159	465	8	472	13	466	15
TT40	No30a37	Tnl	25	Z36-C	0·1183	0·0021	1·1088	0·0298	721	13	758	20	—	—
TT40	No30a38	Tnl	25	Z37-C	0·4470	0·0078	9·5458	0·2569	2382	42	2392	64	2391	49
TT40	No30a39	Tnl	25	Z40-C	0·2959	0·0050	5·1114	0·1354	1671	28	1838	49	—	—
TT40	No30a40	Tnl	25	Z41-C	0·2281	0·0038	3·5458	0·0940	1325	22	1538	41	—	—
TT40	No30a41	Tnl	25	Z43-C	0·1776	0·0030	1·7829	0·0473	1054	18	1039	28	1048	30
TT40	No30a42	Tnl	25	Z45-C	0·3427	0·0058	6·8892	0·1826	1900	32	2097	56	—	—
TT40	No30a43	Tnl	25	Z45-R	0·3037	0·0050	4·5792	0·1216	1709	28	1746	46	1732	42
TT40	Ma14a05	Tnl	10	Z1-R	0·3644	0·0061	6·1382	0·1399	2003	34	1996	45	1995	40
TT40	Ma14a06	Tnl	10	Z5-R	0·0901	0·0018	0·8327	0·0315	556	11	615	23	—	—
TT40	Ma14a07	Tnl	10	Z5-R	0·0789	0·0014	0·6155	0·0191	489	9	487	15	489	17
TT40	Ma14a08	Tnl	10	Z8-R	0·0837	0·0015	1·2396	0·0360	518	9	819	24	—	—
TT40	Ma14a09	Tnl	10	Z6-R	0·1672	0·0028	1·6500	0·0373	997	17	990	22	992	28
TT40	Ma14a10	Tnl	10	Z20-R	0·0798	0·0015	0·6346	0·0186	495	9	499	15	496	17
TT40	Ma14a11	Tnl	10	Z26-R	0·0794	0·0015	0·6223	0·0261	493	9	491	21	493	18
TT40	Ma14a12	Tnl	10	Z30-R	0·0795	0·0015	0·7553	0·0261	493	9	571	20	—	—
TT40	Ma14a13	Tnl	10	Z38-R	0·0497	0·0008	0·4372	0·0098	313	5	368	8	—	—

(continued)

Table 11: Continued

Sample	Run	Rock type	Spot (μm)	Grain-position	$^{206}Pb/^{238}U$	1σ	$^{207}Pb/^{235}U$	1σ	Apparent ages (Ma)					
									$^{206}Pb/^{238}U$	1σ	$^{207}Pb/^{235}U$	1σ	Concordia age	2σ
TT40	Ma14a14	Tnl	10	Z43-R	0·0961	0·0016	0·8826	0·0220	592	10	642	16	—	—
TT40	Ma14a15	Tnl	10	Z37-R	0·1158	0·0019	1·5050	0·0335	707	12	932	21	—	—
TT354	No29a05	Bt-gns	25	Z1-C	0·5042	0·0083	12·8748	0·2992	2632	44	2671	62	2675	43
TT354	No29a06	Bt-gns	25	Z2-C	0·4703	0·0078	11·1533	0·2590	2485	41	2536	59	—	—
TT354	No29a07	Bt-gns	25	Z3-I	0·0971	0·0017	0·7959	0·0210	597	10	595	16	596	19
TT354	No29a08	Bt-gns	25	Z3-I	0·0981	0·0017	0·8007	0·0220	604	10	597	16	602	19
TT354	No29a09	Bt-gns	25	Z3-R	0·0869	0·0015	0·6905	0·0173	537	9	533	13	536	18
TT354	No29a10	Bt-gns	25	Z4-R	0·0986	0·0017	0·8121	0·0196	606	11	604	15	605	19
TT354	No29a11	Bt-gns	25	Z5-C	0·1014	0·0016	1·0571	0·0248	623	10	732	17	—	—
TT354	No29a12	Bt-gns	25	Z6-R	0·1237	0·0020	1·4149	0·0328	752	12	895	21	—	—
TT354	No29a13	Bt-gns	25	Z7-C	0·4423	0·0074	10·4774	0·2452	2361	39	2478	58	—	—
TT354	No29a14	Bt-gns	25	Z10-C	0·1102	0·0019	0·8837	0·0210	674	11	643	15	—	—
TT354	No29a15	Bt-gns	25	Z11-C	0·1733	0·0030	1·7399	0·0465	1030	18	1023	27	1027	31
TT354	No29a16	Bt-gns	25	Z12-C	0·0678	0·0011	0·6400	0·0150	423	7	502	12	—	—
TT354	No29a17	Bt-gns	25	Z13-C	0·1335	0·0023	1·3508	0·0329	808	14	868	21	—	—
TT354	No29a18	Bt-gns	25	Z14-C	0·1147	0·0019	1·1233	0·0265	700	12	765	18	—	—
TT354	No29a19	Bt-gns	25	Z15-C	0·1969	0·0033	2·0329	0·0480	1159	20	1127	27	—	—
TT354	No29a20	Bt-gns	25	Z16-C	0·0946	0·0016	0·7286	0·0172	583	10	556	13	—	—
TT354	No29a24	Bt-gns	25	Z18-C	0·1647	0·0028	1·6176	0·0388	983	16	977	23	980	28
TT354	No29a25	Bt-gns	25	Z22-C	0·1233	0·0022	1·0977	0·0311	750	14	752	21	750	25
TT354	No29a26	Bt-gns	25	Z22-R	0·0901	0·0015	0·7305	0·0170	556	9	557	13	556	17
TT354	No29a27	Bt-gns	25	Z25-C	0·4297	0·0074	8·3335	0·1969	2304	40	2268	54	2264	43
TT354	No29a28	Bt-gns	25	Z26-R	0·4535	0·0079	9·7561	0·2349	2411	42	2412	58	2412	44
TT354	No29a29	Bt-gns	25	Z27-C	0·2095	0·0035	3·6186	0·0852	1226	21	1554	37	—	—
TT354	No29a30	Bt-gns	25	Z30-C	0·1767	0·0030	1·6108	0·0390	1049	18	974	24	—	—
TT354	No29a31	Bt-gns	25	Z31-C	0·1386	0·0023	1·2499	0·0301	837	14	823	20	831	25
TT354	No29a32	Bt-gns	25	Z32-C	0·1216	0·0021	1·0801	0·0260	740	13	744	18	741	23
TT354	No29a33	Bt-gns	25	Z32-R	0·0772	0·0013	0·7078	0·0166	479	8	543	13	—	—
TT354	No29a34	Bt-gns	25	Z33-C	0·0983	0·0017	0·8164	0·0222	605	10	606	16	605	19
TT354	No29a35	Bt-gns	25	Z34-C	0·2499	0·0042	5·1716	0·1212	1438	24	1848	43	—	—
TT354	No29a36	Bt-gns	25	Z34-C	0·3784	0·0064	8·0761	0·1898	2069	35	2240	53	—	—
TT354	No29a37	Bt-gns	25	Z34-C	0·5273	0·0088	13·9219	0·3263	2730	46	2744	64	2746	44
TT354	No29a38	Bt-gns	25	Z35-R	0·4920	0·0084	13·6571	0·3255	2579	44	2726	65	—	—
TT354	No29a39	Bt-gns	25	Z36-C	0·1486	0·0025	1·6407	0·0390	893	15	986	23	—	—
TT354	No29a40	Bt-gns	25	Z36-R	0·1807	0·0031	1·8619	0·0443	1071	18	1068	25	1069	30

Grain-position: C, core; I, intermediate; R, rim. —, discordant; Tnl, tonalite; Bt-gns, biotite gneiss.

The LREE enrichment and strong Ti depletion resemble those of melts calculated from clinopyroxene-II. The melt in equilibrium with green amphibole shows a marked negative Sr anomaly, compatible with the later crystallization of green amphibole and plagioclase relative to clinopyroxene-II. Nb–Ta contents are higher than in the melt computed from clinopyroxene-II whereas lower Zr–Hf values are observed. The Nb_N/Ta_N ratio is below unity.

The two melts computed from the matrix assemblage share many peculiar similarities (e.g. extreme LREE enrichment, Ti and HREE depletion) but also differences that contrast with crystallization of clinopyroxene-II and green amphibole from the same liquid. The higher Cr and Ni contents in green amphibole contrast with the textural evidence of its late crystallization relative to clinopyroxene-II. This evidence and the optical continuity between the two amphibole types indicate that green amphibole

Table 12: Representative zircon trace element composition (ppm)

Rock type:	Qtz-Di	Qtz-Di	Qtz-Di	Qtz-Di	Qtz-Di	Tnl	Tnl	Tnl	Tnl	Tnl	Tnl	Bt-gns	Bt-gns	Bt-gns	Bt-gns	Bt-gns	Bt-gns
Sample:	TT329	TT329	TT329	TT329	TT329	TT40	TT40	TT40	TT40	TT40	TT40	TT354	TT354	TT354	TT354	TT354	TT354
Crystal no.:	Z7	Z8	Z15	Z27	Z11	Z5	Z5	Z5	Z6	Z26	Z29	Z4	Z3	Z1	Z22	Z25	Z36
Age (Ma):	482	520	503	481	483	526	892	489	1078	493	1099	598	533	2693	750	2243	1063
Ti	<10.81	9.77	2.7	<2.67	6.98	11.1	9.16	8.35	3.37	<8.52	4.65	12.3	24.7	9.84	2.08	<5.75	12.0
Sr	0.342	0.994	0.571	0.784	0.748	<0.30	0.225	<0.19	0.935	0.25	1.036	0.398	0.44	0.278	1.07	0.27	2.97
Y	707	383	247	467	275	317	221	107	654	153	1490	286	429	1217	3805	1045	1822
Nb	4.07	2.06	2.08	2.36	2.18	1.95	1.37	1.46	4.83	1.41	1.46	2.53	3.14	2.82	4.33	6.12	6.40
La	0.53	<0.001	0.029	0.866	64.0	0.125	0.168	<0.061	2.05	<0.070	0.867	0.08	<0.098	0.615	0.519	<0.084	0.832
Ce	10.1	9.7	5.2	12.0	276	1.15	1.41	1.05	17.3	2.53	8.13	39.7	17.8	12.5	11.8	44.7	19.5
Pr	0.271	0.09	0.0218	0.212	16.7	<0.043	0.100	<0.023	1.02	0.041	0.776	0.147	0.105	0.534	1.077	0.153	0.449
Nd	2.16	0.327	0.71	1.33	57.0	<0.17	0.642	0.24	5.57	<0.168	5.46	2.16	0.93	4.61	13.3	1.65	2.78
Sm	2.48	0.94	0.75	1.74	4.19	0.75	2.32	<0.087	3.54	0.47	6.33	2.27	1.37	6.28	22.0	4.11	5.28
Eu	0.720	0.424	0.252	0.277	0.511	<0.025	0.089	<0.079	0.416	0.214	0.755	0.728	0.088	0.414	2.46	0.690	0.372
Gd	10.4	6.37	4.72	5.91	4.75	4.56	11.5	1.29	17.5	3.65	36.4	7.79	6.40	28.3	124	21.5	28.3
Tb	3.69	2.30	1.14	2.21	1.41	1.50	3.22	0.48	4.8	0.606	12.56	2.16	2.74	8.61	37.9	8.13	10.7
Dy	53.8	28.9	19.6	35.3	19.5	23.5	31.3	7.52	57.9	10.8	145	25.7	38.7	108	410	94.1	156
Ho	20.5	11.3	7.87	14.0	7.98	10.1	6.86	3.28	22.4	4.86	44.6	9.59	14.9	37.7	131	34.7	57.6
Er	115	61.9	42.0	72.2	45.3	48.6	19.3	18.3	101	28.7	183	41.0	70.0	174	545	169	298
Tm	25.3	15.7	10.3	18.1	12.5	13.3	3.09	5.56	21.6	7.93	34.6	9.07	16.5	36.7	99.1	32.2	64.2
Yb	264	182	123	191	152	131	21.1	61.4	190	87.9	302	102	156	325	791	316	560
Lu	62.6	34.0	22.6	36.9	29.3	27.6	3.5	16.3	38.0	22.9	52.3	20.7	32.5	55.5	131	59.5	113
Hf	10237	8584	8745	9781	8360	7451	8855	7627	8495	8054	7636	8408	8115	7130	8414	9783	9463
Ta	0.750	0.933	0.588	1.01	1.16	1.22	0.611	0.426	1.26	0.678	0.524	0.622	0.874	0.88	1.05	3.21	4.51
Pb	6.70	6.34	2.87	8.18	2.47	2.92	5.66	1.74	8.29	2.02	11.5	21.5	4.08	34.8	33.0	85.1	36.2
Th	161	123	46.2	157	38.8	38.4	51.0	20.0	67.7	26.7	82.3	347	36.6	110	485	289	412
U	266	312	142	411	225	390	618	294	73	232	612	334	551	170	497	790	1164
Eu/Eu*	0.23	0.23	0.18	0.15	0.25	—	0.03	—	0.08	0.20	0.07	0.31	0.05	0.05	0.07	0.11	0.04

Qtz-Di, quartz diorite; Tnl, tonalite; Bt-gns, biotite gneiss.

may be a reaction product partially replacing brown amphibole, and may thus not represent a liquidus phase. The textural evidence for the early crystallization of clinopyroxene-II among the matrix minerals led us to consider the sole melt in equilibrium with clinopyroxene II (hereafter melt-II) to represent the parental melt of the matrix mineral assemblage. The melt computed from clinopyroxene-II does not record the crystallization of plagioclase, thus suggesting that it is not affected by the late precipitation of accessory phases (e.g. titanite, apatite and zircon).

MELT-I: HMA WITH SANUKITIC AFFINITY

Melt-I has clinopyroxene as a liquidus phase, followed by amphibole. Plagioclase is not a liquidus phase. The relatively high Cr contents (up to 2000 ppm) and Mg-number (0·84) of clinopyroxene-I are consistent with a mantle origin. This is also consistent with the brown amphibole compositions (Cr = 1100 ppm, Ni = 410 ppm and Mg-number = 0·74). According to the K_dCpx/liquid$^{Fe/Mg}$ exchange coefficients for pressure conditions of 0·5–1·0 GPa (Gudfinnsson & Presnall, 2000), the molar Mg-number of melt-I is inferred to be up to 0·62. Although melt-I records a fractional crystallization process of mafic minerals, its incompatible trace element pattern is considered to retain significant information about the geochemical signature of the primary mantle melt.

Clinopyroxene-I chemistry suggests crystallization from a melt with relatively low Al_2O_3, Na_2O and TiO_2 and relatively high MgO and Cr_2O_3. Calculated equilibrium melts have low HREE, Y, Zr, Hf and Ti and exceptionally high B, Pb, Th and U contents relative to N-MORB, indicating that melt-I is not a common arc magma, of either oceanic or continental setting. The major element composition of clinopyroxene-I resembles that of clinopyroxenes in mafic intrusive rocks crystallized from HMA (Fig. 4). In particular, close similarities are

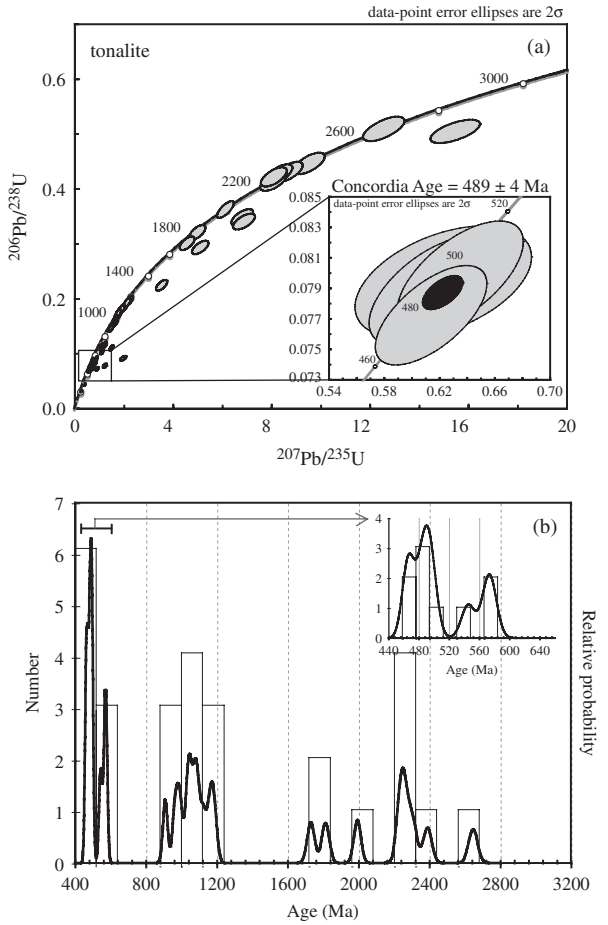

Fig. 12. Geochronological results for the tonalite. (a) $^{238}U/^{206}Pb$ vs $^{235}U/^{207}Pb$ concordia diagram. (b) Cumulative probability density plot of U–Pb concordia ages. The inset represents a close-up of the 440–640 Ma age range.

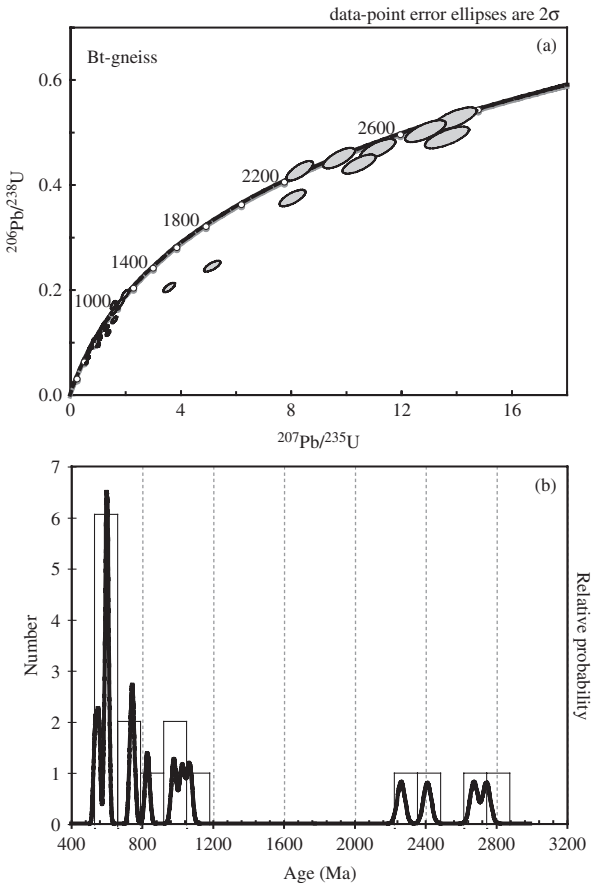

Fig. 13. Geochronological results for the Bt-gneiss. (a) $^{238}U/^{206}Pb$ vs $^{235}U/^{207}Pb$ concordia diagram. (b) Cumulative probability density plot of U–Pb concordia ages.

observed to the clinopyroxenes from Cambrian quartz melagabbros with boninitic affinity from the Glenelg River Complex (SE Australia; Kemp, 2003, 2004) and to clinopyroxene from the Early Cretaceous high-Mg diorites with sanukitic affinity from Kyushu (SW Japan; Kamei *et al.*, 2004). Chemical analogies are also found with the clinopyroxenes from the evolved intrusive products (gabbronorites) of the adjacent Niagara Icefall mafic–ultramafic complex with boninite affinity (Tribuzio *et al.*, 2007).

Although the low HREE, Y, Zr, Hf and Ti contents suggest a boninite affinity, Melt-I cannot be considered a typical boninite (e.g. Taylor *et al.*, 1994), because of the absence of orthopyroxene as liquidus phase, the slightly higher HREE contents and the LREE, Th, Nb enrichment relative to HREE (Fig. 15). HMA with boninite affinity but variably enriched in LREE and LILE have been reported elsewhere in the Delamerian Orogen: in the Heathcoat Greenstone Belt of Central Victoria (Australia; Crawford & Cameron, 1985) and in the Heat Creek Bed formation in New Zealand (Münker & Cooper, 1999). However, in both cases orthopyroxene is still a major mafic mineral. Striking chemical similarities are observed between melt-I and the HMA sanukitoids from the Setouchi Volcanic Belt (Tatsumi & Ishizaka, 1982; Shimoda *et al.*, 1998; Fig. 15). A peculiar feature of the sanukitoids with respect to boninites is the rare occurrence of orthopyroxene and the presence of mafic minerals such as biotite ± amphibole ± clinopyroxene (Martin *et al.*, 2005). We therefore propose a close relationship between melt-I from the Husky Ridge and sanukitic melts.

The petrogenesis of melt-I is suggested to involve a refractory mantle that accounts for the low HREE, Zr, Hf and Ti contents and an agent rich in H_2O, B, Th, U, LREE and Nb. Marine terrigenous sediments, which are recycled at convergent margins, are a realistic source for the addition of H_2O, Th, U, LREE and possibly Nb and B into the mantle (Plank & Langmuir, 1998; Plank, 2005). Direct partial melting of the sedimentary cover of the slab, or sediment transfer into the hot zone of the mantle wedge through buoyancy or subduction erosion and consequent melting (Goss & Kay, 2006), may induce the percolation of a sediment-derived melt into the mantle wedge.

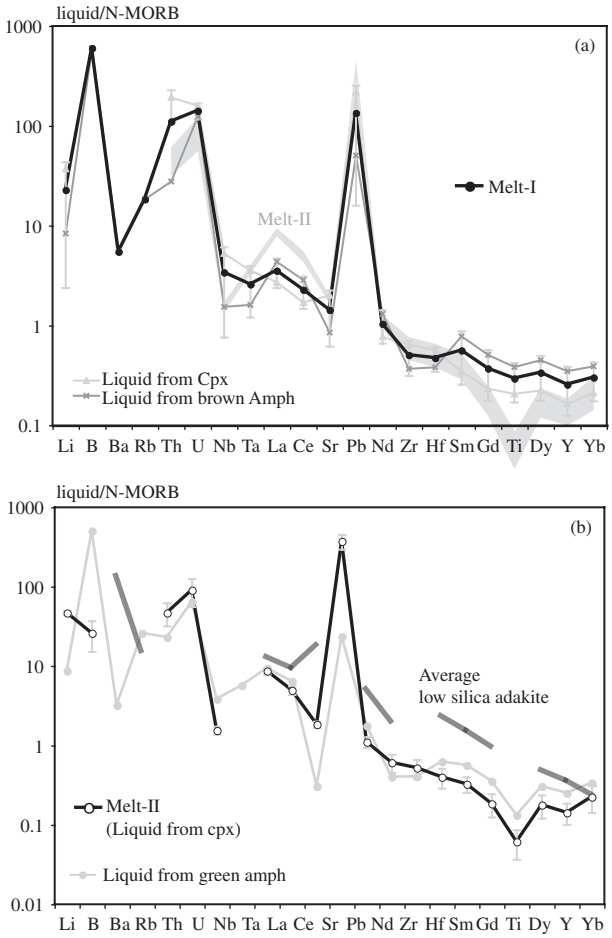

Fig. 14. N-MORB normalized incompatible element pattern of computed melt from quartz diorites obtained by applying $D^{S/L}$ (Electronic Appendix 2) to the average mineral composition. (a) Liquids computed from clinopyroxene-I and brown amphibole. Melt-I composition is the average of the melts computed from clinopyroxene-I and brown amphibole. Melt-II composition is shown for comparison as a light grey field. (b) Liquids computed from clinopyroxene-II (Melt-II) and green amphibole. Average low-silica adakite composition (Martin *et al.*, 2005) is shown for comparison. N-MORB values for normalization are from GERM (http://earthref.org). Error bars are 2σ errors.

The partial melting of a highly refractory mantle wedge reacted and equilibrated with a sediment-derived hydrous melt may thus account for the trace element composition of melt-I. This process is basically that proposed to account for the petrogenesis of the sanukitic HMA of the Setouchi Volcanic Belt (e.g. Shimoda *et al.*, 1998).

MELT-II: EVOLVED SANUKITOID BY AMPHIBOLE CRYSTALLIZATION

The lower Cr_2O_3 contents and Mg-number of clinopyroxene-II than clinopyroxene-I, the higher Si/Al ratio of green amphibole than brown amphibole, the presence of accessory quartz and the Na-rich composition of plagioclase (An up to 35 mol %) suggest that melt-II is more evolved than melt-I. The high LILE contents and the marked negative Nb–Ta anomaly are evidence for a subduction component. Similarly to melt-I, however, the trace element signature is different from that of common arc lavas. Among subduction-related melts, marked LREE/HREE fractionation and low HREE contents are typical of adakites ($La_N/Yb_N > 10$; $Yb < 1{\cdot}8$ ppm; Defant & Drummond, 1990). In addition, the composition of green amphibole indicates that melt-II possesses a Nb_N/Ta_N ratio lower than unity, which is also a compositional feature of adakitic melts (e.g. Foley *et al.*, 2002). The lack of olivine and the presence of clinopyroxene as an early crystallizing mineral are also consistent with an adakitic origin. However, the low HREE contents, the negative Ti anomaly and the U-shaped HREE pattern contrast with a typical adakite (Fig. 14). In addition, the Sr content of melt-II (about 210 ppm) is lower than that of typical adakites (Sr > 400 ppm; Defant & Drummond, 1990).

Table 13: Trace element composition (ppm) of liquids in equilibrium with mineral phases

	Cpx-I	Brown Amph	Cpx-II	Green Amph
Li	223	50.1	279	52.1
B	—	540	23	451
Ba	—	45.0	—	26.3
Rb	—	13.4	—	18.9
Th	31.6	4.54	7.67	3.76
U	10.4	8.03	5.84	4.17
Nb	16.0	4.65	4.68	11.6
Ta	0.60	0.27		0.97
La	8.79	14.1	28.2	30.4
Ce	16.6	27.8	48.3	62.4
Sr	230	98.1	211	35.0
Pb	106	24.7	182	11.4
Nd	7.29	12.4	10.4	16.7
Zr	61.4	35.3	58.4	38.6
Hf	1.51	1.02	1.39	1.08
Sm	1.18	2.67	1.36	2.13
Eu	0.50	0.95	0.43	0.75
Gd	1.18	2.58	0.93	1.79
Ti	1757	3256	518	1127
Dy	1.32	2.66	1.05	1.80
Y	6.06	12.9	5.26	9.24
Yb	0.84	1.55	0.89	1.33

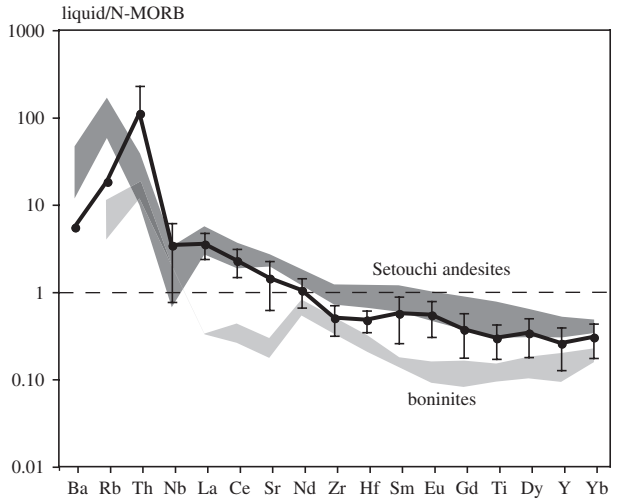

Fig. 15. N-MORB normalized incompatible element pattern of melt-I compared with that of the Setouchi andesites (Tatsumi & Ishizaka, 1982; Shimoda *et al.*, 1998) and boninites (Taylor *et al.*, 1994). N-MORB values for normalization are from GERM (http://earthref.org).

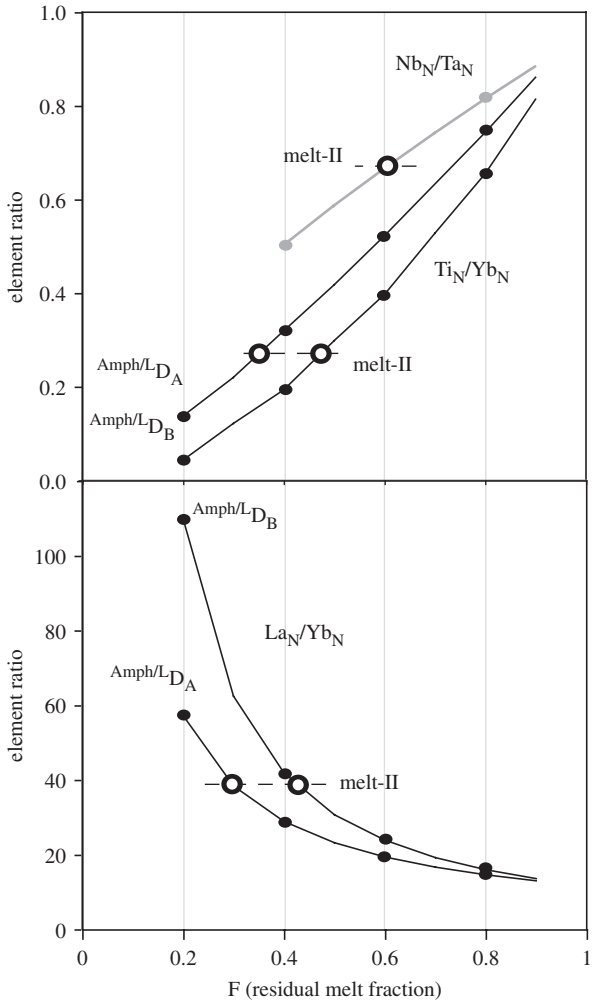

Fig. 16. Modelling of the variation of Nb_N/Ta_N, Ti_N/Yb_N and La_N/Yb_N element ratios as a function of residual melt fraction (F) after amphibole crystallization starting from melt-I composition. Simulation was carried out considering two sets of $D^{Amph/L}$ ($D_A^{Amph/L}$ $D_B^{Amph/L}$; Electronic Appendix 2). ○, target values (melt-II). Elements are normalized to N-MORB (GERM: http://earthref.org).

The steep REE pattern is a relatively uncommon geochemical signature that can be used to constrain the petrogenesis of melt-II. The LREE/HREE fractionation in adakites is commonly attributed to the partial melting of the subducted slab under eclogite-facies conditions, leaving garnet in the solid residue (Drummond & Defant, 1990; Martin *et al.*, 2005, and references therein). However, it has been shown that other processes are capable of producing melts with steep REE patterns; that is, partial melting of the lower crust (Petford & Atherton, 1996; Xu *et al.*, 2002; Chung *et al.*, 2003; Garrison & Davidson, 2003; Stevenson *et al.*, 2005) and melt differentiation through crystallization of garnet-bearing assemblages at mantle or crustal levels (Macpherson *et al.*, 2006; Rodriguez *et al.*, 2007). In the following sections, we explore the role that the crust and fractional crystallization may have played in producing the geochemical signature of melt-II.

The crustal contribution

The presence of inherited 'old' zircons (at 666 ± 19 Ma) in quartz diorites and the relatively high abundance of trace elements with crustal affinity such as Rb, LREE and Th in melt-II indicate the involvement of a crustal component in their petrogenesis. However, a pure crustal origin for melt II is unlikely. Crustal melts from the lower basaltic crust have generally lower Mg-number (close to 0·30; Rapp & Watson, 1995) than that inferred for melt-II (about 0·52–0·56). Therefore, Melt-II may have originated by hybridization of melt-I with upper crustal acid liquids as suggested for the similar Mg-rich rocks with boninitic affinity from the Glenelg River Complex in the Delamerian Orogen (SE Australia; Kemp, 2004). At Glenelg River petrographic evidence, such as intermingling with two-mica leucogranite and the local presence of ocellar textures, showed that the parental melt of the quartz melagabbros was variably hybridized by felsic magmas of crustal origin. At the Husky Ridge, no peraluminous leucogranite is exposed and no ocellar textures, alkali feldspar and white mica occur in quartz diorites.

Despite the lack of relations between quartz diorites and tonalites in the exposed crustal section, the occurrence of the tonalitic body a few tens of meters distant from the quartz diorites does not allow us to exclude an *a priori* a role of the tonalitic melt as hybridizing agent.

However, the mineral assemblage of the tonalite and that of the matrix assemblage in the quartz diorites are different. Clinopyroxene, one of the major matrix minerals in the quartz diorites, is absent in the tonalites and the opposite holds for biotite. Green amphibole from the tonalite is significantly richer in Fe and HREE (Mg-number = 0·5; Y ~88 ppm) than green amphibole from quartz diorites (Mg-number = 0·7; Y ~13 ppm). In addition, opposite LREE fractionation trends characterize the two amphiboles. The abundance of inherited zircons from the host basement in the tonalite and their near-total absence in the quartz diorites is further evidence against a direct link between the tonalite and melt II.

A petrogenetic process controlled by crustal contamination for the origin of the geochemical signature of melt-II is also unlikely. Because the mean continental crust is about two times higher in HREE and Zr than melt-II (Rudnick & Fountain, 1995), a substantial crustal contribution is unable to yield melts with the observed low HREE concentrations. Furthermore, to produce a melt with high La_N/Yb_N ratios (up to 38), a mineral phase such as garnet, capable of strongly fractionating LREE from HREE, should remain in the solid residue. Nevertheless, the concave-upward HREE pattern of melt-II contrasts with residual garnet, which would produce melts with high Dy/Yb ratios.

Differentiation through amphibole crystallization

The LREE enrichment and Ti depletion of melt-II may have been acquired through differentiation by fractional crystallization at crustal levels. The low HREE, the relatively high Mg-number, and the high Th and U contents common to both melt-II and melt-I indicate a genetic relationship. The hypothesis that melt-II is a differentiated product of melt-I is thus explored. In particular, because melt-II lacks the garnet signature, a process dominated by amphibole crystallization is hypothesized.

A fractional crystallization process driven by amphibole was simulated starting from melt-I and using two different sets of $D^{Amph/L}$ (Electronic Appendix 3): (1) those previously adopted for melt computation ($D_A^{Amph/L}$); (2) a set reporting higher compatibility for HREE [$D_B^{Amph/L}$; the highest among those reported by Tiepolo *et al.* (2007)]. As discussed above, the more evolved nature of melt-II with respect to melt-I may justify the choice of slightly higher $D^{S/L}$ for the elements with high $\mathcal{Z}/r$ ratios. Furthermore, because a fractional crystallization process dominated by amphibole separation causes a SiO_2 enrichment in the residual melt, the $D^{Amph/L}$ values are expected to increase during the differentiation process. Results for Ti_N/Yb_N and the La_N/Yb_N ratio are reported in Fig. 16. A mean residual melt fraction around 30% accounts for the trace element variation between melt-I and melt-II using $D_A^{Amph/L}$, whereas a residual melt fraction of about 40% is obtained with the $D_B^{Amph/L}$ set of partition coefficients. Amphibole crystallization is therefore able to produce the three times increase of the La_N/Yb_N ratio in the residual melt and the negative Ti anomaly in the incompatible element pattern. The same modelling holds for the origin of the U-shaped pattern of melt-II.

The significantly lower Nb_N/Ta_N ratio of the melt in equilibrium with green amphibole relative to that of the melt in equilibrium with brown amphibole also supports amphibole crystallization for the origin of melt-II. Among the major rock-forming minerals, only amphibole was demonstrated to prefer Nb with respect to Ta (Tiepolo *et al.*, 2000*b*). According to equation (2) of Tiepolo *et al.* (2000*b*) and the amphibole composition in Amph-gabbros, the $D_{Nb}^{Amph/L}/D_{Ta}^{Amph/L}$ ratio is around 1·7. The crystallization of either brown or green amphibole may lead to a decrease of the Nb/Ta ratio in the residual melt. A model of the Nb_N/Ta_N evolution in residual melt after brown amphibole fractional crystallization indicates that, starting from melt-I, the Nb/Ta ratio of melt-II can be accounted with a residual melt fraction of about 60% (Fig. 16). This residual melt fraction is slightly lower than that inferred from La_N/Yb_N and Ti_N/Yb_N modelling. However, because of the uncertainties related to $D^{S/L}$ values and those intrinsic into the Nb/Ta modelling (about 7–20%; Tiepolo *et al.*, 2000*b*), we maintain that the results are essentially similar.

The early crystallization of clinopyroxene among matrix minerals (i.e. the amphibole replacement by clinopyroxene as a liquidus phase) is not fully consistent with an evolution of melt-II by continuous amphibole crystallization. There are, however, different possible explanations for the early crystallization of clinopyroxene in melt-II. The crystallization of large amounts of amphibole requires a melt capable of supplying the necessary H_2O for the whole process. The stability of amphibole is also controlled by dehydrogenation [i.e. the incorporation of less H_2O than the stoichiometry (e.g. Tiepolo *et al.*, 1999)], which may occur when high-charge cations such as Ti or Fe^{3+} are available to balance the charge deficit. Because of the relatively high compatibility of Ti in amphibole, however, Ti is rapidly depleted as the melt evolves. A low H_2O content coupled with low Ti concentrations may thus inhibit amphibole crystallization and enhance that of clinopyroxene. Alternatively, heating during decompression crystallization (Blundy *et al.*, 2006; Davidson *et al.*, 2007) may shift the system away from the restricted thermal stability field of amphipbole and enhance the crystallization of clinopyroxene.

THE PETROGENETIC MODEL: A SUMMARY

Textural and chemical evidence prevents the quartz diorites of the Husky Ridge from being considered as a

closed system in terms of fractional crystallization and two different melt injections must be invoked in the petrogenetic process. The first melt injection (melt-I) has a sanukitic affinity, is rich in H_2O and lacks plagioclase as an early liquidus phase. It formed by partial melting of a refractory mantle equilibrated with silicic melts derived from partial melting of the sediment cover of the subducted slab, similar to the Setouchi andesites (Shimoda *et al.*, 1998). Melt-I stalls, cools and crosses the amphibole-in phase boundary at mid-crustal levels (i.e. ~5 kbar; Castelli *et al.*, 2003). The growth and accumulation of large brown amphibole at the expense of the early crystallizing clinopyroxene is thus enhanced. The crystal mush dominated by brown amphibole is subsequently injected by a residual melt (melt-II) with plagioclase at the liquidus and characterized by strong LREE enrichment and Ti depletion. As a consequence of this interaction, the pre-existing brown amphibole is variably replaced by a new generation of amphibole (green amphibole) with the trace element signature typical of melt-II. The peculiar trace element signature of melt-II is acquired through amphibole crystallization starting from a sanukitic melt similar to melt-I, which probably occurred in a deeper magma chambers. Heating of the magma during decompression crystallization (e.g. Blundy *et al.*, 2006) and/or the unavailability of enough H_2O and Ti for brown amphibole stability may have caused the replacement at the liquidus of amphibole with clinopyroxene.

TECTONIC IMPLICATIONS

The intrusion of the Husky Ridge quartz diorites occurred at mid-crustal levels during the Mid-Cambrian (~515 Ma). The U–Pb zircon ages from the Bt-gneiss, showing peaks at the major Pan-African events of accretion of Gondwana, confirm that the basement rocks belong to the Gondwana active margin (i.e. the Wilson Terrane), in agreement with Castelli *et al.* (2003).

The sanukitic intrusion of the Husky Ridge has no equal in the Ross orogenic belt in Antarctica. Major compositional differences are observed with respect to the mafic rocks of the Terra Nova Intrusive Complex and Teall Nunatak intrusion, ranging in age from 510 to 480 Ma (Di Vincenzo & Rocchi, 1999; Dallai *et al.*, 2003; Rocchi *et al.*, 2004; Giacomini *et al.*, 2007). Geochemical affinities are observed with the nearby mid-Cambrian mafic–ultramafic Niagara Icefall Complex of boninitic affinity (Tribuzio *et al.*, 2007), as a refractory mantle is required to account for the low HREE, Y, Zr and Hf in both complexes. The absence of orthopyroxene as a liquidus phase, the abundant amphibole at the liquidus, and the enrichment in LILE and LREE suggest that the parental melts of the Husky Ridge intrusion were not typical boninites. Heterogeneous migration and release of the sediment-derived melts from the subducted slab in the highly refractory mantle may be at the centre of these differences. Both the Husky Ridge and Niagara Icefall intrusive sequences require a high heat flux to promote the second-stage melting of the refractory mantle. In particular, the Husky Ridge intrusion shows that the heat flux also induced partial melting in the sediment cover of the subducted slab.

The partial melting of the subducted slab during the Ross–Delamerian Orogeny has been already proposed. Small intrusive bodies with adakitic affinity ranging in age from 516 ± 10 to 531 ± 10 Ma were reported in south Victoria Land (Allibone & Wysoczanski, 2002). The involvement of melts from the sediment cover of the slab was indicated by the study of Ol-bearing cumulates from the Teall Nunatak Intrusion (NVL) dated at 521 ± 2 Ma (Giacomini *et al.*, 2007). Furthermore, the presence of intrusive products recording melts from the subducted slab was reported in the Delamerian Orogen (e.g. the Glenelg River Complex, SE Australia; Kemp, 2004). On the basis of present data, we propose that the slab melting process was nearly synchronous across Victoria Land. Slab roll-back was proposed as a possible explanation for the abrupt termination at the end of the Cambrian of convergent deformation throughout the Ross–Delamerian Orogen, followed by buoyant uplift, exhumation and post-collisional magmatism (e.g. Foden *et al.*, 2006, and references therein). The influx of new asthenosphere as a result of slab roll-back is also a suitable mechanism to supply heat at the regional scale required for the partial melting of both the subducted slab sediments and the subcontinental mantle previously depleted by melt extraction.

CONCLUDING REMARKS ON THE ROLE OF AMPHIBOLE IN ARC MAGMAS

The Husky Ridge quartz diorites are evidence for the occurrence at mid-crustal levels of cumulus rocks in which amphibole may be up to 90% in volume and for the open-system evolution of subduction-related magmas within the crust. The products of a poorly evolved melt and those of a residual liquid after amphibole crystallization coexist at chemical disequilibrium at the thin-section scale. This work shows that the absence of amphibole among the liquidus phases of a residual melt (e.g. melt-II) does not preclude that it has crystallized at deeper crustal levels (see Davidson *et al.*, 2007). Useful geochemical markers to detect the cryptic amphibole crystallization are: (1) the U-shaped pattern of HREE; (2) the Nb_N/Ta_N ratios below unity; (3) the negative Ti anomaly with respect to HREE.

According to the petrogenetic process proposed for melt-II, amphibole fractionation alone may account for the marked LREE enrichment and HREE depletion

(i.e. adakitic signature) observed in some arc lavas and the involvement of garnet is not required. In particular, high proportions of amphibole (~50%) are capable of shifting the La_N/Yb_N ratio towards significantly high values (up to 39), which are three times those of the parental melt.

The quartz diorites from the Husky Ridge are an example of how amphibole-rich mafic bodies may act as reservoir for the H_2O storage in the crust. Based on the data reported by Tiepolo *et al.* (2000*a*), a mean exchange coefficient for H_2O between pargasitic amphibole and melt can be assumed to be close to 0·3. According to this value and the amphibole modal proportions (up to 90 vol. %), quartz diorites from the Husky Ridge can subtract up to 27% of H_2O from the parental mantle melt. In addition, considering that primitive arc magma may have H_2O content up to 5% (Wallace, 2005), quartz diorites may be a crustal reservoir for up to 1·4% of H_2O.

ACKNOWLEDGEMENTS

Stefania Fiameni provided very generous support in zircon preparation and characterization by CL and LA-ICPMS. Alberto Zanetti is gratefully acknowledged for the stimulating discussion. Luigi Dallai shared with us the emotion of the Husky Ridge sampling during the 20th Italian Antarctic expedition and also sacrificed his camera for science. Claudio Ghezzo is gratefully acknowledged for having introduced us into the Antarctic world. The manuscript benefited by the constructive reviews of T. Kemp, A. F. Cooper and P. T. Leat. The editor John Gamble is also gratefully acknowledged. The PNRA is thanked for having funded the purchase of the LA-ICPMS system.

SUPPLEMENTARY DATA

Supplementary data for this paper are available at *Journal of Petrology* online.

REFERENCES

Allibone, A. & Wysoczanski, R. (2002). Initiation of magmatism during the Cambrian–Ordovician Ross orogeny in southern Victoria Land, Antarctica. *Geological Society of America Bulletin* **114**, 1007–1018.

Anders, E. & Ebihara, M. (1982). Solar system abundances of the elements. *Geochimica et Cosmochimica Acta* **46**, 2363–2380.

Black, L. P. & Sheraton, J.W. (1990). The influence of Precambrian source components on the U–Pb zircon age of a Palaeozoic granite from Northern Victoria Land, Antarctica. *Precambrian Research* **46**, 275–293.

Blundy, J. D. & Shimizu, N. (1991). Trace element evidence for plagioclase recycling in calc-alkaline magmas. *Earth and Planetary Science Letters* **102**, 178–197.

Blundy, J., Cashman, K. & Humphreys, M. (2006). Magma heating by decompression-driven crystallisation beneath andesite volcanoes. *Nature* **443**, 76–80.

Boger, S. D. & Miller, J. McL. (2004). Terminal suturing of Gondwana and the onset of the Ross–Delamerian orogeny: the cause and effect of an Early Cambrian reconfiguration of plate motions. *Earth and Planetary Science Letters* **219**, 35–48.

Bomparola, R. M., Ghezzo, C., Belousova, E., Griffin, W. L. & O'Reilly, S. Y. (2007). Resetting of the U–Pb zircon system in Cambro-Ordovician intrusives of the Deep Freeze Range, northern Victoria Land, Antarctica. *Journal of Petrology* **48**, 327–364.

Borg, S. C. & De Paolo, D. J. (1991). A tectonic model of the Antarctic Gondwana margin with implication for southeastern Australia: isotopic and geochemical evidence. *Tectonophysics* **196**, 339–358.

Castelli, D., Oggiano, G., Talarico, F., Belluso, E. & Colombo, F. (2003). Mineral chemistry and petrology of the Wilson Terrane metamorphics from Retreat Hills to Lady Newnes Bay, northern Victoria land, Antarctica. *Geologisches Jahrbuch* **85**, 135–171.

Cawthorn, G. R. (1996). Models for incompatible trace element abundances in cumulus minerals and their application to plagioclase and pyroxenes in the Bushveld complex. *Contributions to Mineralogy and Petrology* **123**, 109–115.

Chung, S.-L., Liu, D., Ji, J., Chu, M.-F., Lee, H.-Y., Wen, D.-J., Lo, C.-H., Lee, T.-Y., Qian, Q. & Zhang, Q. (2003). Adakites from continental collision zones: melting of thickened lower crust beneath south Tibet. *Geology* **31**, 1021–1024.

Cooper, R. A. & Tulloch, A. J. (1992). Early Palaeozoic terranes in New Zeland and their relationships to the Lachlan Fold Belt. *Tectonophysics* **214**, 129–144.

Crawford, A. J. & Cameron, W. E. (1985). Petrology and geochemistry of Cambrian boninites and low-Ti andesites from Heatcote, Victoria. *Contributions to Mineralogy and Petrology* **91**, 93–104.

Crawford, A. J., Falloon, T. J. & Green, D. H. (1989). Classification, petrogenesis and tectonic setting of boninites. In: Crawford, A. J. (ed.) *Boninites and Related Rocks*. London: Unwin Hyman, pp. 2–44.

Dallai, L., Ghezzo, C. & Sharp, Z. D. (2003). Oxygen isotope evidence for crustal assimilation and magma mixing in the Granite Harbour Intrusives, Northern Victoria Land, Antarctica. *Lithos* **67**, 135–151.

Davidson, J., Turner, S., Handley, H., Macpherson, C. & Dosseto, A. (2007). Amphibole 'sponge' in arc crust? *Geology* **35**, 787–790.

Defant, M. J. & Drummond, M. S. (1990). Derivation of some modern arc magmas by melting of young subducted lithosphere. *Native* **347**, 662–665.

Diethelm K. (1985). Hornblendite und Gabbros im ostichen Bergell (Val Sissone, Provinz Sondrio, Italien). *Schweizerische Mineralogische und Petrographische Mitteilungen* **65**, 223–246.

Di Vincenzo, G. & Rocchi, S. (1999). Origin and interaction of mafic and felsic magmas in an evolving late orogenic setting: the Early Paleozoic Terra Nova Intrusive Complex, Antarctica. *Contributions to Mineralogy and Petrology* **137**, 15–35.

Di Vincenzo, G., Palmeri, R., Talarico, F., Andriessen, P. A. M. & Ricci, C. A. (1997). Petrology and geochronology of eclogites from the Lanterman Range, Antarctica. *Journal of Petrology* **38**, 1391–1417.

Di Vincenzo, G., Carosi, R., Palmri, R. & Tiepolo, M. (2007). A comparative U–Th–Pb (zircon–monazite) and ^{40}Ar–^{39}Ar (muscovite–biotite) study of shear zones in northern Victoria Land (Antarctica): implications for geochronology and localized reworking of the Ross Orogen. *Journal of Metamorphic Geology* **25**, 605–630.

Drummond, M. S. & Defant, M. J. (1990). A model for trondhjemite–tonalite–dacite genesis and crustal growth via slab melting: Archean to modern comparisons. *Journal of Geophysical Research* **95**, 21503–21521.

Federico, L., Capponi, G. & Crispini, L. (2006). The Ross orogeny of the Transantarctic Mountains: a Northern Victoria Land perspective. *International Journal of Earth Sciences* **95**, 759–770.

Foden, J., Elburg, M., Dougherty-Page, J. & Burtt, A. (2006). The timing and duration of the Delamerian orogeny: correlation with the Ross Orogen and implications for the Gondwana assembly. *Journal of Geology* **114**, 189–210.

Foley, S., Tiepolo, M. & Vannucci, R. (2002). Growth of early continental crust controlled by melting of amphibolite in subduction zones. *Nature* **417**, 837–840.

Foster, D. A., Gray, D. R. & Spaggiari, C. (2005). Timing of subduction and exhumation along the Cambrian East Gondwana margin, and the formation of the Palaeozoic backarc basins. *Geological Society of America Bulletin* **117**, 105–116.

Garrido, C. J., Bodinier, J.-L., Burg, J.-P., Zeilinger, G., Hussain, S. S., Dawood, H., Chaudhry, M. N. & Gervilla, F. (2006). Petrogenesis of mafic garnet granulite in the lower crust of the Kohistan Palaeo-arc Complex (Northern Pakistan): implications for intracrustal differentiation of island arcs and generation of continental crust. *Journal of Petrology* **47**, 1873–1914.

Garrison, J. M. & Davidson, J. P. (2003). Dubious case for slab melting in the Northern Volcanic Zone of the Andes. *Geology* **31**, 565–568.

Giacomini, F., Tiepolo, M., Dallai, L. & Ghezzo, C. (2007). On the onset and evolution of the Ross orogeny magmatism in North Victoria Land—Antarctica. *Chemical Geology* **240**, 103–128.

Goss, A. R. & Kay, S. M. (2006). Steep REE patterns and enriched Pb isotopes in southern Central American arc magmas: evidence for forearc subduction erosion? *Geochemistry, Geophysics, Geosystems* **7**, doi:10.1029/2005GC001163.

Greene, A. R., DeBari, S. M., Kelemen, P. B., Blusztajn, J. & Clift, P. D. (2006). A detailed geochemical study of island arc crust: the Talkeetna arc section, south–central Alaska. *Journal of Petrology* **47**, 1051–1093.

Gudfinnsson, G. & Presnall, D. C. (2000). Melting behaviour of model lherzolite in the system $CaO–MgO–Al_2O_3–SiO_2–FeO$ at 0·7–2 GPa. *Journal of Petrology* **41**, 1241–1269.

Gunn, G. M. & Warren, G. (1962). Geology of Victoria Land between Mawson and Mullock Glaciers, Antarctica. *New Zealand Geological Survey Bulletin* **71**, 85–100.

Horstwood, M. S. A., Foster, G. L., Parrish, R. R., Noble, S. R. & Nowell, G. M. (2003). Common-Pb corrected *in situ* U–Pb accessory mineral geochronology by LA-MC-ICP-MS. *Journal of Analytical Atomic Spectrometry* **18**, 837–846.

Jagoutz, O., Müntener, O., Burg, J.-P., Ulmer, P. & Jagoutz, E. (2006). Lower continental crust formation through focused flow in km-scale melt conduits: The zoned ultramafic bodies of the Chilas Complex in the Kohistan arc (NW Pakistan). *Earth and Planetary Science Letters* **320**, 320–342.

Kamei, A., Owada, M., Nagao, T. & Shiraki, K. (2004). High-Mg diorites derived from sanukitic HMA magmas, Kyushu Island, southwest Japan arc: evidence from clinopyroxene and whole rock compositions. *Lithos* **75**, 359–371.

Kemp, A. I. S. (2003). Plutonic boninite-like rocks in an anatectic setting: Tectonic implications for the Delamerian orogen in southeastern Australia. *Geology* **31**, 371–374.

Kemp, A. I. S. (2004). Petrology of high-Mg, low-Ti igneous rocks of the Glenelg River Complex (SE Australia) and the nature of their interaction with crustal melts. *Lithos* **78**, 119–156.

Ketchum, J. W. F., Jackson, S. E., Culshaw, N. G. & Barr, S. M. (2001). Depositional and tectonic setting of the Paleoproterozoic Lower Aillik Group, Makkovik Province, Canada: evolution of a passive margin–foredeep sequence based on petrochemistry and U–Pb (TIMS and LAM-ICP-MS) geochronology. *Precambrian Research* **105**, 331–356.

Ludwig, K. R. (2000). *Isoplot—a Geochronological Toolkit for Microsoft Excel. Berkeley Geochronology Center, Special Publications* **1a**, 53 pp.

Macpherson, C. G., Dreher, S. T. & Thirlwall, M. F. (2006). Adakites without slab melting: High pressure differentiation of island arc magma, Mindanao, the Philippines. *Earth and Planetary Science Letters* **243**, 581–593.

Martin, H., Smithies, R. H., Rapp, R., Moyen, J.-F. & Champion, D. (2005). An overview of adakite, tonalite–trondhjemite–granodiorite (TTG), and sanukitoid: relationships and some implications for crustal evolution. *Lithos* **79**, 1–24.

Meert, J. G. (2003). A synopsis of events related to the assembly of eastern Gondwana. *Tectonophysics* **362**, 1–40.

Münker, C. & Cooper, R. (1999). The Cambrian arc complex of Takaka Terrane, New Zealand: an integrated stratigraphical, paleontological and geochemical approach. *New Zealand Journal of Geology and Geophysics* **42**, 415–445.

Münker, C. & Crawford, A. (2000). Cambrian arc along the SE Gondwana active margin: a synthesis from Tasmania–New Zealand–Australia–Antarctica correlations. *Tectonics* **19**, 415–432.

Musumeci, G. (1999). Magmatic belts in accretionary margins, a key for tectonic evolution: the Tonalite Belt of North Victoria land (East Antarctica). *Journal of the Geological Society, London* **156**, 177–189.

Pearce, J. A., van der Laan, S. R., Arculus, R. J., Murton, B. J., Ishii, T., Peate, D. W. & Parkinson, I. J. (1992). Boninite and harzburgite from LEG125 (Bonin–Mariana Forearc): a case study of magma genesis during the initial stages of subduction. In: Fryer, P., Pearce, J. A. & Stokking, L. B. (eds) *Proceedings of the Ocean Drilling Program, Scientific Results, 125.* College Station, TX: Ocean Drilling Program, pp. 623–657.

Petford, N. & Atherton, M. (1996). Na-rich partial melts from newly underplated basaltic crust: the Cordillera Blanca Batholith, Peru. *Journal of Petrology* **37**, 1491–1521.

Plank, T. (2005). Constraints from thorium/lanthanum on sediment recycling at subduction zones and the evolution of the continents. *Journal of Petrology* **46**, 921–944.

Plank, T. & Langmuir, C. H. (1998). The chemical composition of subducting sediment and its consequences for the crust and mantle. *Chemical Geology* **145**, 325–394.

Rapp, R. P. & Watson, E. B. (1995). Dehydration melting of metabasalt at 8–32 kbar: implications for continental growth and crust–mantle recycling. *Journal of Petrology* **36**, 891–931.

Rocchi, S., Tonarini, S., Armienti, P., Innocenti, F. & Manetti, P. (1998). Geochemical and isotopic structure of the early Paleozoic active margin of Gondwana in northern Victoria Land, Antarctica. *Tectonophysics* **284**, 261–281.

Rocchi, S., Di Vincenzo, G. & Ghezzo, C. (2004). The Terra Nova Intrusive Complex (Victoria Land, Antarctica). *Terra Antarctica Reports* **10**, 49 pp.

Rodriguez, C., Selles, D., Dungan, M., Langmuir, C. & Leeman, W. (2007). Adakitic dacites formed by intracrustal crustal fractionation of water-rich parent magmas at nevado de Longavi Volgano (36·2°S; Andean Southern Volcanic Zone, Central Chile). *Journal of Petrology* **48**, 2033–2061.

Rubatto, D. (2002). Zircon trace element geochemistry: partitioning with garnet and the link between U–Pb ages and metamorphism. *Chemical Geology* **184**, 123–138.

Rudnick, R. L. & Fountain, D. M. (1995). Nature and composition of the continental crust—a lower crustal perspective. *Reviews in Geophysics* **33**, 267–309.

Shimoda, G., Tatsumi, Y., Nohda, S., Ishizaka, K. & Jahn, B.M. (1998). Setouchi high-Mg andesites revisited: geochemical evidence for melting of subducted sediments. *Earth and Planetary Science Letters* **160**, 479–492.

Stevenson, J. A., Daczko, N. R., Clarke, G. L., Pearson, N. & Klepeis, K. A. (2005). Direct observation of adakite melts generated in the lower continental crust, Fiordland, New Zeland. *Terra Nova* **17**, 73–79.

Stump, E. (1995). *The Ross Orogen of the Transantarctic Mountains.* Cambridge: Cambridge University Press, 284 pp.

Tatsumi, Y. & Ishizaka, K. (1982). Origin of high-magnesian andesites in the Setouchi volcanic belt southwest Japan, I. Petrographical and chemical characterisation. *Earth and Planetary Science Letters* **60**, 293–304.

Taylor, R. N., Nesbitt, R. W., Vidal, P., Harmon, R. S., Auvray, B. & Croudace, I. W. (1994). Mineralogy, chemistry, and genesis of the Boninite Series Volcanics, Chichijima, Bonin Islands, Japan. *Journal of Petrology* **35**, 577–617.

Tessensohn, F. & Henjes-Kunst, F. (2005). Northern Victoria Land terranes, Antarctica: far-travelled or local products? In: Vaughan, A. P. M., Leat, P. T. & Pankhurst, R. J. (eds) *Terrane Processes at the Margins of Gondwana. Geological Society, London, Special Publications* **296**, 275–291.

Tiepolo, M. (2003). *In situ* Pb geochronology of zircon with laser ablation–inductively coupled plasma–sector field mass spectrometry. *Chemical Geology* **199**, 159–177.

Tiepolo, M. & Tribuzio, R. (2005). Slab-melting during Alpine orogeny: evidence from mafic cumulates of the Adamello batholith (Central Alps, Italy). *Chemical Geology* **216**, 271–288.

Tiepolo, M., Zanetti, A. & Oberti, R. (1999). Detection, crystal-chemical mechanisms and petrological implications of $^{[6]}Ti^{4+}$ partitioning in pargasite and kaersutite. *European Journal of Mineralogy* **11**, 345–354.

Tiepolo, M., Vannucci, R., Bottazzi, P., Oberti, R., Zanetti, A. & Foley, S. F. (2000*a*). Partitioning of REE, Y, Th, U and Pb between pargasite, kaersutite and basanite to trachyte melts: implications for percolated and veined mantle. *Geochemistry, Geophysics, Geosystems* **1**, paper number 2000GC000064.

Tiepolo, M., Vannucci, R., Oberti, R., Foley, S., Bottazzi, P. & Zanetti, A. (2000*b*). Nb and Ta incorporation and fractionation in titanian pargasite and kaersutite: crustal-chemical constraints and implications for natural systems. *Earth and Planetary Science Letters* **176**, 185–200.

Tiepolo, M., Tribuzio, R. & Vannucci, R. (2002). The composition of mantle-derived melts developed during the Alpine continental collision. *Contributions to Mineralogy and Petrology* **144**, 1–15.

Tiepolo, M., Oberti, R., Zanetti, A., Vannucci, R. & Foley, S. F. (2007). Amphiboles: crystal chemistry, occurence, and health issues. In: Hawthorne, F. C., Oberti, R., Della ventura, G. & Mottana, A. (eds) *Mineralogical Society of America, Reviews in Mineralogy and Geochemistry* **67**, 417–452.

Tribuzio, R., Tiepolo, M., Vannucci, R. & Bottazzi, P. (1999). Trace element distribution within olivine-bearing gabbros from northern Apennine ophiolites (Italy): evidence for post-cumulus crystallisation in MOR-type gabbroic rocks. *Contributions to Mineralogy and Petrology* **134**, 123–133.

Tribuzio, R., Tiepolo, M. & Fiameni, S. (2007). A mafic–ultramafic cumulate sequence derived from boninite-type melts (Niagara Icefall, northern Victoria Land, Antarctica). *Contributions to Mineralogy and Petrology* doi:10.1007/s00410-007-0261-1.

van Achterbergh, E., Ryan, C. G., Jackson, S. E. & Griffin, W. (2001). Data reduction software for LA-ICP-MS. In: Sylvester, P. (ed.) *Laser Ablation-ICPMS in the Earth Science. Mineralogical Association of Canada. Short course series* **29**, 239–243.

Vavra, G., Gebauer, D., Schmid, R. & Compston, W. (1996). Multiple zircon growth and recrystallisation during polyphase Late Carboniferous to Triassic metamorphism in granulites of the Ivrea Zone (Southern Alps): an ion microprobe (SHRIMP) study. *Contributions to Mineralogy and Petrology* **122**, 337–358.

Vita-Scaillet, G. & Lombardo, B. (2003). Biotite K/Ar Ages of metamorphic rocks of the Retreat Hills, Meander Glacier and Mountaineer Range, Northern Victoria Land Antarctica. In: Tessensohn, F. & Ricci, C. A. (eds) *Aspects of a Suture Zone. Mariner Glacier Area, Antarctica. Geologisches Jahrbuch, Polar Issue No. 9*, pp. 173–193.

Wallace, P. J. (2005). Volatiles in subduction zone magmas: concentrations and fluxes based on melt inclusion and volatile gas data. *Journal of Volcanology and Geothermal Research* **140**, 217–240.

Widenbeck, M., Alle, P., Corfu, F., Griffin, W. L., Meier, M., Ober, F., Von Quant, A., Roddick, J. C. & Spiegel, J. (1995). Three natural zircon standards for U–Th–Pb, Lu–Hf, trace element and REE analysis. *Geostandandards Newsletter* **19**, 1–23.

Xu, J.-F., Shinjo, R., Defant, M. J., Wang, Q. & Rapp, R. P. (2002). Origin of Mesozoic adakitic rocks in the Ningzhen area of east China: partial melting of delaminated lower continental crust? *Geology* **30**, 1111–1114.